

# Classical bilayer crystals of dipoles

Xin Lu<sup>1</sup> and Chang-Qin Wu<sup>1</sup>

<sup>1</sup>*Department of Physics, Fudan University, Shanghai 200433, China*

Andrea Micheli<sup>2,3</sup> and Guido Pupillo<sup>2,3</sup>

<sup>2</sup>*Institute for Theoretical Physics, University of Innsbruck, A-6020 Innsbruck, Austria*

<sup>3</sup>*Institute for Quantum Optics and Quantum Information of the Austrian Academy of Sciences, A-6020 Innsbruck, Austria*

We study the structure and melting of a classical bilayer system of dipoles, in a setup where the dipoles are oriented perpendicular to the planes of the layers and the density of dipoles is the same in each layer. Due to the anisotropic character of the dipole-dipole interactions, we find that the ground-state configuration is given by two hexagonal crystals positioned on top of each other, independent of the interlayer spacing and dipolar density. For large interlayer distances these crystals are independent, while in the opposite limit of small interlayer distances the system behaves as a two-dimensional crystal of paired dipoles. Within the harmonic approximation for the phonon excitations, the melting temperature of these crystalline configurations displays a non-monotonic dependence on the interlayer distance, which is associated with a *re-entrant* melting behavior in the form of *solid-liquid-solid-liquid* transitions at fixed temperature.

PACS numbers: 68.65.Ac Multilayers, 61.50.-f Crystalline state, 52.27.Lw Dusty or complex plasmas; plasma crystals, 82.70.Dd Colloids, 64.70.Dv Solid-liquid transitions

## I. INTRODUCTION

The realization of a degenerate dipolar gas of <sup>52</sup>Cr atoms<sup>1,2</sup> and the experimental progress in the realization of cold molecular ensembles<sup>3</sup> have spurred interest in the properties of particles with large dipole moments<sup>4,5,6,7,8,9,10,11,12</sup> in atomic and molecular setups<sup>13</sup>. In particular, the strong anisotropic dipole-dipole interactions induced in ground-state polar molecules by external electric fields hold promises for applications ranging from the realization of novel strongly-correlated phases<sup>14,15,16,17,18,19,20,21,22,23,24,25,26,27,28,29,30,31,32,33,34</sup> to quantum simulations<sup>35,36,37</sup> and quantum computing<sup>38,39,40,41,42,43</sup>.

In Refs.<sup>12,29</sup> it is shown that a collisionally stable two-dimensional (2D) setup where particles interact via *purely repulsive* effective dipole-dipole interactions can be realized by polarizing the molecules using an external electric field, and thus inducing strong dipole-dipole interactions, and by confining the motion of the particles to a 2D geometry, e.g. by trapping them into a single well of a deep optical lattice directed parallel to the electric field. The low-energy phase of an ensemble of interacting bosonic polar molecules is then a superfluid or a self-assembled crystal for comparatively weak and strong interactions, respectively, where the strength of the interactions can be modified by varying the intensity of the polarizing electric field. The crystal is a two-dimensional hexagonal lattice structure with quantum dynamics given by longitudinal and transverse acoustic phonons. Contrary to familiar Wigner crystals induced by strong Coulomb interactions<sup>44</sup>, dipolar crystals emerge at large densities, where dipole-dipole interactions dominate over the kinetic energy of the particles. This scenario for the realization of 2D crystals can be

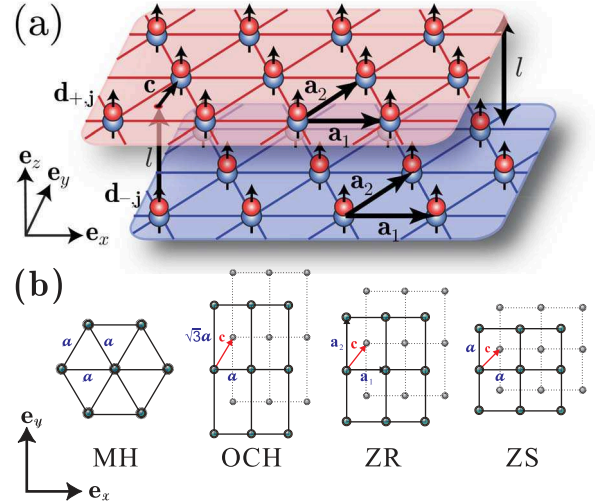


FIG. 1: (Color online) (a) Sketch of the system setup depicting the dipolar bi-layer system: The dipoles are oriented along the  $z$  direction,  $\mathbf{d} = d\mathbf{e}_z$ , and confined to two  $(x, y)$  planes separated by an interlayer distance  $l$  along the  $z$  direction. The intralayer dipole-dipole repulsion gives rise to a crystalline structure in each layer with basis vectors  $\mathbf{a}_i$ , here illustrated by two hexagonal structures with an in-plane displacement  $\mathbf{c}$ . (b) Various possible equilibrium geometries for the bilayer crystal, shown as a projection onto the  $(x, y)$  plane. From left to right: a matching hexagonal (MH) configuration, a one-component hexagonal (OCH) configuration, a zigzag rectangular configuration with aspect ratio  $a_2/a_1$  (ZR), and a zigzag square (ZS) configuration. The position of the dipoles and their nearest-neighbor links in the upper (lower) layer are shown by solid (dashed) circles and lines, respectively. A detailed summary of the lattice parameters is given in Table I.

implemented using closed-shell polar molecules as, e.g.,

SrO or RbCs.

While the scenario above is realized by populating a single well of the confining optical lattice, in general it will be possible to populate more than one well of the lattice. It is thus natural to consider the phases of bi- and multilayer configurations of classical and quantum dipoles. As a first step, in this work we focus on the crystalline structures of a bilayer system of classical dipoles. The analogous quantum problem will be the subject of a separate study.

In this paper we consider a system of  $2N$  dipoles confined into two parallel two-dimensional planes along the  $(x, y)$ -directions, separated by an interlayer spacing  $l$  along  $z$ . Each plane has the same number of dipoles,  $N$ , with their dipole-moment  $\mathbf{d} = d\mathbf{e}_z$  aligned perpendicular to the plane, see Fig. 1(a). The interactions between two dipoles separated by  $\mathbf{r}$  are the dipole-dipole interactions  $V(\mathbf{r}) = d^2[1 - 3z^2/r^2]/r^3$ , where  $r = |\mathbf{r}| > 0$  and  $z = \mathbf{r} \cdot \mathbf{e}_z$ . For our setup this results in the intra-layer interactions being always repulsive, which gives rise to a hexagonal crystalline structure in each layer. In contrast, the inter-layer interactions are attractive (repulsive) for dipoles separated by a distance  $r < \sqrt{3}l$  ( $r > \sqrt{3}l$ ), see Fig. 1(a). As detailed in the following sections this anisotropy in the inter-layer interactions determines that the groundstate configuration of the system is a bilayer crystal comprised of two hexagonal crystals stacked on top of each other. In addition, it gives rise to a non-monotonic behavior of the dynamic properties of this bilayer crystal (such as the phonon sound velocities and the melting temperature) when increasing the interlayer distance  $l$ , while keeping the intra-layer densities  $n$  fixed. In particular, within the harmonic approximation for the phonon excitations we find that for certain fixed temperatures the system displays a *reentrant* melting behavior in the form of *solid-liquid-solid-liquid* transitions as a function of the dimensionless inter-layer distance  $\xi = l\sqrt{n}$ . The picture emerging from these studies is one where for large interlayer separations  $\xi \gg 1$  the two hexagonal crystals of the bilayer structure behave as independent crystals, while for vanishing inter-layer separations  $\xi \ll 1$  they behave as a single 2D crystal of particles with double mass and double dipole-moment.

The paper is organized as follows: In Section II we introduce our model and derive expressions for the potential energy in the form of a rapidly convergent sum obtained via the Ewald summation method. By comparing the energies of a number of possible crystal geometries, we determine the structure and energy of the ground-state and of several excited-state configurations. In Section III we analyze the dynamic properties corresponding to these crystalline structures within the harmonic approximation for the phonon excitations. We discuss the phonon excitation branches of the ground-state configuration and we find that the dependence of the sound-velocities on the inter-layer separation  $l$  is

non-monotonic, due to the anisotropic character of the dipole-dipole interaction. For the excited-states we assess the stability of the configurations studied in Sec. II under phonon fluctuations and find that several of the excited states are meta-stable. In Section IV we study the thermal melting of the bilayer-crystal. We derive the classical melting temperature  $T_m$  via a modified two-dimensional Lindemann criterion, and find that the temperature  $T_m$  behaves non-monotonically with increasing inter-layer distance.

## II. GROUND AND EXCITED STATES

We consider a system of *classical* dipoles confined into two planes along the  $x - y$  direction, separated by a distance  $l$  along  $z$ . We focus on the situation where the dipole-moments  $\mathbf{d}_i$  of the particles are aligned perpendicular to the planes, i.e. along  $z$ , and where one has the same density  $n$  of dipoles in each layer, see Fig. 1(a). The interactions between two dipoles is given by their dipole-dipole interactions  $V(\mathbf{r}) = d^2[1 - 3z^2/r^2]/r^3$ , where  $r = |\mathbf{r}| > 0$  is their distance and  $z = \mathbf{r} \cdot \mathbf{e}_z$  their interlayer distance. We note that the dipole-dipole interactions are long-range, i.e. decaying like  $1/r^3$  and anisotropic in space. At zero-temperature the system is in a crystalline configuration, where the particles in each layer form a 2D crystal, and the relative position of the particles is correlated by the long-range dipole-dipole interaction. We denote the 2D position of the dipoles within the upper (lower) layer by  $\mathbf{R}_{+,j}$  ( $\mathbf{R}_{-,j}$ ), which we parameterize by

$$\mathbf{R}_{\pm,j} = j_1 \mathbf{a}_1 + j_2 \mathbf{a}_2 \pm \mathbf{c}/2, \quad (1)$$

where the integers  $j \equiv (j_1, j_2)$  label the  $j^{\text{th}}$  particle in each layer,  $\mathbf{a}_1$  and  $\mathbf{a}_2$  are the basis vectors of the periodic structure with density  $n$  and  $\mathbf{c}$  is a two-dimensional vector accounting for a relative in-plane displacement of the two structures, see Fig. 1(a).

The interactions are given by

$$V = \frac{1}{2} \sum_{\sigma=\pm} \sum_{j \neq j'} \frac{d^2}{|\mathbf{R}_{\sigma,j} - \mathbf{R}_{\sigma,j'}|^3} + \sum_{j,j'} \frac{d^2 (|\mathbf{R}_{+,j} - \mathbf{R}_{-,j}|^2 - 2l^2)}{(|\mathbf{R}_{+,j} - \mathbf{R}_{-,j}|^2 + l^2)^{5/2}}, \quad (2)$$

where the first (second) term describes the intra-layer (inter-layer) interactions. Since the intra-layer interactions do not depend on the inter-layer separation  $l$ , it is convenient to split the energy per dipole,  $E$ , into its intra- and inter-layer part as  $E = V/2N = E_0 + E_I$ . Making use of the translational invariance of the infinite system the two contributions read

$$E_0 = \frac{1}{2} \sum_{j \neq 0} \frac{d^2}{|\mathbf{R}_j|^3}, \quad (3a)$$

$$E_I = \frac{1}{2} \sum_j \frac{d^2 (|\mathbf{R}_j + \mathbf{c}|^2 - 2l^2)}{(|\mathbf{R}_j + \mathbf{c}|^2 + l^2)^{5/2}}, \quad (3b)$$

TABLE I: Lattice parameters of four considered configurations: the matching hexagonal (MH), the one-component hexagonal (OCH), the zigzag rectangular (ZR) and a zigzag square (ZS). From left to right:  $\mathbf{a}_1$  and  $\mathbf{a}_2$  are the primitive vectors,  $\mathbf{c}$  is the inter-lattice displacement vector,  $\mathbf{b}_1$  and  $\mathbf{b}_2$  are the primitive translation vectors of the reciprocal lattice and  $n$  is the density of each layer. We introduced the vector notation  $(x, y) \equiv x\mathbf{e}_x + y\mathbf{e}_y$  for the two-dimensional components; the lattice constant is  $a \equiv |\mathbf{a}_1|$  and  $a_2/a_1$  denotes the aspect ratio for ZR configuration.

lattice	$\mathbf{a}_1/a$	$\mathbf{a}_2/a$	$2\mathbf{c}$	$\mathbf{b}_1 a/2\pi$	$\mathbf{b}_2 a/2\pi$	$na^2$
MH	(1, 0)	$(\frac{1}{2}, \frac{\sqrt{3}}{2})$	0	$(1, \frac{-1}{\sqrt{3}})$	$(0, \frac{2}{\sqrt{3}})$	$\frac{2}{\sqrt{3}}$
OCH	(1, 0)	$(0, \sqrt{3})$	$(1, \sqrt{3})$	(1, 0)	$(0, \frac{1}{\sqrt{3}})$	$\frac{1}{\sqrt{3}}$
ZS	(1, 0)	(0, 1)	(1, 1)	(1, 0)	(0, 1)	1
ZR	(1, 0)	$(0, \frac{a_2}{a_1})$	$(1, \frac{a_2}{a_1})$	(1, 0)	$(0, \frac{a_1}{a_2})$	$\frac{a_1}{a_2}$

where  $\mathbf{R}_j \equiv \mathbf{R}_{\sigma,j} - \mathbf{R}_{\sigma,0} = j_1\mathbf{a}_1 + j_2\mathbf{a}_2$  denote the relative (2D) positions of the dipoles in each layer. Given the slow convergence of the sum in real space involved in Eq. (3), we use the Ewald summation method to obtain an expression for  $E$  involving rapidly convergent sums. The explicit derivation is given in Appendix A. We here provide only the derived expressions for  $E_0$  and  $E_I$ , which read

$$\begin{aligned} \frac{E_0}{d^2} = & \pi n \sum_j \left[ \frac{4\alpha}{\sqrt{\pi}} e^{-|\mathbf{G}_j|^2/4\alpha^2} - 2|\mathbf{G}_j| \operatorname{erfc} \left( \frac{|\mathbf{G}_j|}{2\alpha} \right) \right] \\ & + \sum_{j \neq 0} \left[ \frac{\operatorname{erfc}(\alpha|\mathbf{R}_j|)}{|\mathbf{R}_j|^3} + \frac{2\alpha}{\sqrt{\pi}} \frac{e^{-\alpha^2|\mathbf{R}_j|^2}}{|\mathbf{R}_j|^2} \right] - \frac{4\alpha^3}{3\sqrt{\pi}}, \end{aligned} \quad (4a)$$

$$\begin{aligned} \frac{E_I}{d^2} = & \pi n \sum_j e^{i\mathbf{G}_j \cdot \mathbf{c}} \left[ \frac{4\alpha}{\sqrt{\pi}} e^{-|\mathbf{G}_j|^2/4\alpha^2 - \alpha^2 l^2} \right. \\ & \left. - |\mathbf{G}_j| \sum_{\pm} e^{\pm i\mathbf{G}_j l} \operatorname{erfc} \left( \frac{|\mathbf{G}_j|}{2\alpha} \pm \alpha l \right) \right] + \\ & \sum_j \left[ \frac{\operatorname{erfc}(\alpha|\tilde{\mathbf{R}}_j|)}{|\tilde{\mathbf{R}}_j|^3} \left( 1 - \frac{3l^2}{|\tilde{\mathbf{R}}_j|^2} \right) \right. \\ & \left. + \frac{2\alpha}{\sqrt{\pi}} \frac{e^{-\alpha^2|\tilde{\mathbf{R}}_j|^2}}{|\tilde{\mathbf{R}}_j|^2} \left( 1 - \frac{3l^2}{|\tilde{\mathbf{R}}_j|^2} - 2\alpha^2|\tilde{\mathbf{R}}_j|^2 \right) \right], \end{aligned} \quad (4b)$$

with  $|\tilde{\mathbf{R}}_j| \equiv (|\mathbf{R}_j + \mathbf{c}|^2 + l^2)^{1/2}$ . In Eq. (4)  $n$  denotes the intra-layer density and  $\mathbf{G}_j$  are the 2D reciprocal vectors of a single layer, which are parametrized by  $\mathbf{G}_j = j_1\mathbf{b}_1 + j_2\mathbf{b}_2$  in terms of the primitive translation vectors of the reciprocal lattice  $\mathbf{b}_1$  and  $\mathbf{b}_2$ . The quantity  $\alpha > 0$  is an (arbitrary) inverse length, for which a convenient choice is the inverse of the mean particle separation, i.e.,  $\alpha = 1/r_0 = \sqrt{\pi n}$ .

In order to determine the ground-state configuration, in the following we calculate the energy of a number of possible crystal configurations.

Motivated by the fact that the ground-state for a single layer is given by a hexagonal lattice structure, we first consider a hexagonal structure in each layer with the two structures displaced by  $\mathbf{c}$ , see Fig. 1(a). We find that for an arbitrary inter-layer separation  $l$ , the minimal energy is attained for  $\mathbf{c} = 0$  (modulo the lattice constant). This is also what one would intuitively expect, since the closest dipoles in different layers tend to attract each other, which leads to a locking of the relative positions of the two layers. The attained “matching” hexagonal (MH) structure is illustrated in Fig. 1(b) and its basis and reciprocal vectors are listed in Table I, together with three other (meta-stable) configurations detailed below. In Figure 2 we plot the energy per particle  $E^{(\text{MH})}$  attained for the MH configuration at a fixed density  $n$  as a function of the dimensionless inter-layer separation  $\xi \equiv l/(\sqrt{\pi}r_0)$ , given by the inter-layer distance in units of the mean particle separation (up to a constant  $1/\sqrt{\pi}$ ), as a solid line. We notice that for large inter-layer separations,  $\xi \gg 1$ , the ground-state energy approaches the value corresponding to a single hexagonal (SH) layer in its ground-state, i.e.  $E^{(\text{MH})}(\xi \rightarrow \infty) = E^{(\text{SH})} \approx 4.443d^2n^{3/2}$ . In the opposite limit,  $\xi \ll 1$ , the energy is dominated by the large attraction between the two layers  $E^{(\text{MH})}(\xi \ll 1) \approx (-1/\xi^3 + 2 \times 4.443)d^2n^{3/2}$ , which diverges as  $\propto -1/l^3$  for  $l \rightarrow 0$ , due to the strong attraction of the closest dipoles in different layers. We remark that the latter corresponds to an unphysical regime for typical AMO systems<sup>12</sup>. In fact, at these short distances the required depth of the optical trapping potential for realizing a 2D layer becomes unreasonably large. Moreover one expects short-range interactions in the form of, e.g., Van-der-Waals interactions as well as the core repulsion, to dominate the interactions at these small distances<sup>45</sup>. These latter effects have been neglected in our model, c.f. Eq. (2). However, we notice that here the physically relevant quantity is  $\xi$ , and the limit  $\xi \rightarrow 0$  can be approached by decreasing the density of dipoles  $n$  while keeping  $l$  fixed.

In order to confirm that the MH configuration is the ground-state, we compare its energy to those of a number of other (intuitively motivated) configurations<sup>46</sup>.

As a first alternative configuration we consider a “one component” hexagonal (OCH) structure, which is obtained by removing every second dipole in each layer in a staggered way and rescaling the relative density. The OCH configuration is illustrated in Fig. 1(b), and its basis and reciprocal vectors are summarized in Table I. The attained energy  $E^{(\text{OCH})}$  is plotted in Fig. 2 as a function of  $\xi$  as a dashed-dotted line, and we notice that it exceeds that of the MH configuration. The label OCH has been chosen for this configuration, as it resembles a hexagonal lattice for a single component, when looked from above. Accordingly, in the limit of vanishing inter-lattice separation the energy of the OCH configuration tends to that of a single hexagonal layer (with a double density), i.e.

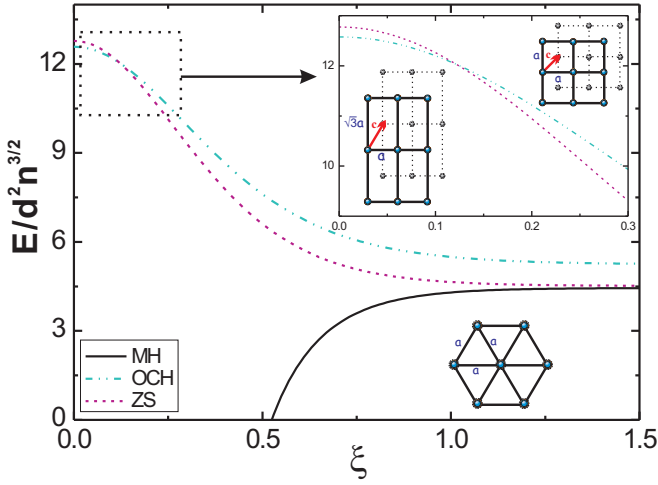


FIG. 2: (Color online) The energy per dipole  $E$  for a fixed density  $n$  as a function of  $\xi$  for three different lattice configurations: MH (solid line), OCH (dash-dotted line) and ZS (dotted line). The inset is a blow-up of the excited state energies in the region of small interlattice separation,  $0 \leq \xi \leq 0.3$ , showing a crossing of the OCH- and ZS-energies around  $\xi \approx 0.12$ .

$$E^{(\text{OCH})}(\xi = 0) \approx 4.443 d^2 (2n)^{3/2} \approx 12.576 d^2 n^{3/2}.$$

As a second alternative configuration we consider a “zig-zag” square (ZS) structure, where dipoles in each layer form a square lattice, and the two layers are shifted with respect to each other as illustrated in Fig. 1. The basis and reciprocal vectors for the ZS structure are given in Table I. The energy for the ZS-structure  $E^{(\text{ZS})}$  is shown in Fig. 2 as a dashed line. The figure shows that for large  $\xi$  the energy of the ZS configuration exceeds the MH energy but it is smaller than the OCH energy, while at small  $\xi$  the energies of the ZS and OCH configurations become comparable. The inset of Fig. 2 is a blow-up of the excited state energies in the region  $0 \leq \xi \leq 0.3$ . From the inset, we observe that the two energies,  $E^{(\text{OCH})}$  and  $E^{(\text{ZS})}$ , actually cross at  $\xi = \xi_0 \approx 0.12$  and for  $\xi < \xi_0$  the OCH structure is energetically favored over the ZS one.

The excited state configurations OCH and ZS can be interpolated smoothly by “stretching” the lattice, which in general leads to a “zig-zag” rectangular (ZR) structure with a variable aspect ratio  $a_2/a_1$  in each layer. The ZR structure is illustrated in Fig. 1(b) and its basis and reciprocal vectors are listed in Table I. In order to find the optimal ZR configuration, we minimize the energy as a function of the free parameter  $a_2/a_1$ . The obtained aspect ratio  $a_2/a_1$  for the optimal ZR configuration is shown in the inset of Fig. 3, and we notice that the resulting structure coincides with the OCH and ZS configurations at  $\xi = 0$  and  $\xi \approx 0.17$ , respectively. The energy obtained for the optimal ZR configuration,  $E^{(\text{ZR})}$ , is plotted as a dashed line in Fig. 3 in the region  $0.05 \lesssim \xi \lesssim 0.17$ , along with the ones obtained for the OCH (dash-dotted line) and ZS structures (dotted line). The figure shows that  $E^{(\text{ZR})}$  equals  $E^{(\text{OCH})}$  and  $E^{(\text{ZS})}$  at  $\xi = 0$  and  $\xi \approx 0.17$ , respectively, while it is lower in the

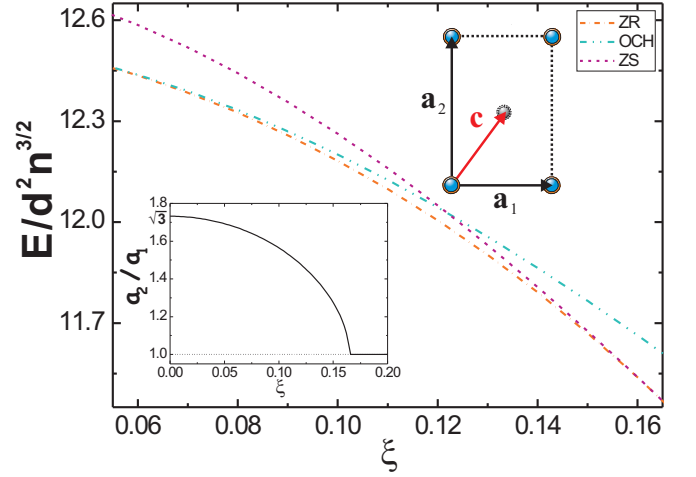


FIG. 3: (Color online) The energy per particle  $E$  as a function of  $\xi$  for the OCH (dash-dotted line), the optimal ZR (dashed line) and ZS configuration (dotted line), showing the transitions: OCH  $\rightarrow$  ZR  $\rightarrow$  ZS with increasing  $\xi$ . Inset: The aspect ratio  $a_2/a_1$  for the ZR-configuration as a function of  $\xi$ .

parameter region in between.

The results above are consistent with the MH configuration being the ground-state of the system for all  $\xi$ , due to the attraction between particles in the two layers (separated by  $r < \sqrt{3}l$ ). This in contrast to the situation occurring for Coulomb bilayer systems, where the repulsion between particles in the different layers leads to a change of the ground-state configuration depending on the ratio of the inter-layer separation to the mean intra-layer spacing<sup>46</sup>. However, we notice that analogous (smooth) transitions between different configurations occur here between excited-state structures, which will be shown below to be metastable. These structures may in principle be prepared using properly-designed in-plane optical lattice potentials, as argued below.

### III. DYNAMICAL PROPERTIES

In this section, we study the phonon spectra for those equilibrium lattice configurations, which we found in the previous section. Thereby we make use of the harmonic approximation of the lattice excitations, and determine the stability (meta-stability) of the obtained configurations for the ground (excited states) under small fluctuations.

In order to obtain the excitation spectra for the various lattice configurations, we consider the dynamical matrix  $\mathbf{M}_D(\mathbf{q})$ , whose eigenvalues are the square of the phonon frequencies<sup>47</sup>. We notice that the bilayer configurations above correspond to a (single 2D) Bravais lattice with a unit cell given by two molecules, one in the upper and



one in the lower layer. Thus  $\mathbf{M}_D(\mathbf{q})$  is here a  $4 \times 4$  matrix

$$\mathbf{M}_D(\mathbf{q}) = \begin{pmatrix} M_{++}^{xx} & M_{++}^{xy} & M_{+-}^{xx} & M_{+-}^{xy} \\ M_{++}^{xy} & M_{++}^{yy} & M_{+-}^{xy} & M_{+-}^{yy} \\ M_{+-}^{xx} & M_{+-}^{xy} & M_{--}^{xx} & M_{--}^{xy} \\ M_{+-}^{xy} & M_{+-}^{yy} & M_{--}^{xy} & M_{--}^{yy} \end{pmatrix}, \quad (5)$$

where the superscript  $\tau = x$  ( $\tau = y$ ) refer to a displacement along  $x$  ( $y$ ) and the subscript  $\sigma = +$  ( $\sigma = -$ ) refer to the components in the upper (lower) layer. The matrix elements in Eq. (5) read

$$M_{\sigma\sigma}^{\tau\nu} \equiv \frac{1}{m} [D_{++}^{\tau\nu}(0) - D_{++}^{\tau\nu}(\mathbf{q}) + D_{+-}^{\tau\nu}(0)], \quad (6a)$$

$$M_{+-}^{\tau\nu} \equiv \frac{1}{m} [-D_{+-}^{\tau\nu}(\mathbf{q})], \quad (6b)$$

where  $m$  is the mass of the dipoles. The quantities  $D_{+\sigma}^{\tau\nu}(\mathbf{q})$  are defined as

$$D_{+\sigma}^{\tau\nu}(\mathbf{q}) = \sum_j e^{-i\mathbf{q} \cdot (\mathbf{R}_{0,+} - \mathbf{R}_{j,\sigma})} \partial_\tau \partial_\nu V_{0+,j\sigma}(\mathbf{r} = 0), \quad (7)$$

with  $V_{0+,j\sigma}(\mathbf{r})$  the two-body interaction potential between the dipole at position 0 in layer  $+$  and the dipole  $j$  in layer  $\sigma$ . At  $\mathbf{q} = 0$  the quantities  $D_{+\sigma}^{\tau\nu}(\mathbf{q})$  for  $\sigma = +$  ( $\sigma = -$ ) correspond to the intra-layer (inter-layer) force constants.

Using the Ewald summation method [see Eq. (A9) and Eq. (A17) in Appendix A], we can rewrite the sum in Eq. (7) into the following rapidly convergent forms

$$D_{++}^{\tau\nu}(\mathbf{q}) = - \sum_j (\mathbf{q} + \mathbf{G}_j)_\tau (\mathbf{q} + \mathbf{G}_j)_\nu \Upsilon \left( \frac{|\mathbf{G}_j + \mathbf{q}|}{2\alpha}, 0 \right) + \frac{8\alpha^5}{5\sqrt{\pi}} \delta_{\tau\nu} + \sum_{j \neq 0} \lim_{\mathbf{r} \rightarrow 0} \partial_\tau \partial_\nu \Omega_1(|\mathbf{R}_j + \mathbf{r}|), \quad (8a)$$

$$D_{+-}^{\tau\nu}(\mathbf{q}) = - \sum_j (\mathbf{q} + \mathbf{G}_j)_\tau (\mathbf{q} + \mathbf{G}_j)_\nu e^{i\mathbf{G}_j \cdot \mathbf{c}} \Upsilon \left( \frac{|\mathbf{G}_j + \mathbf{q}|}{2\alpha}, \alpha l \right) + \sum_j e^{-i\mathbf{q} \cdot (\mathbf{R}_j + \mathbf{c})} \lim_{\mathbf{r} \rightarrow 0} \partial_\tau \partial_\nu \Omega_2(|\tilde{\mathbf{R}}_j + \mathbf{r}|), \quad (8b)$$

where  $\delta_{\tau\nu}$  is the Kronecker-delta, and where we used the notation  $(\mathbf{q} + \mathbf{G}_j)_\tau \equiv \mathbf{e}_\tau \cdot (\mathbf{q} + \mathbf{G}_j)$  for the component in the direction  $\tau$  of the two-dimensional (reciprocal) vectors. The functions  $\Upsilon(x, y)$ ,  $\Omega_1(x)$  and  $\Omega_2(x)$  in Eq. (8)

are given by

$$\Upsilon(x, y) = \frac{4\alpha}{\sqrt{\pi}} e^{-x^2 - y^2} + \sum_{\pm} (\pm 2) \alpha x e^{\pm 2xy} \operatorname{erfc}(x \pm y), \quad (9a)$$

$$\Omega_1(x) = \frac{\operatorname{erfc}(\alpha x)}{x^3} + \frac{2\alpha e^{-\alpha^2 x^2}}{\sqrt{\pi} x^2}, \quad (9b)$$

$$\Omega_2(x) = \frac{\operatorname{erfc}(\alpha x)}{x^3} + \frac{2\alpha e^{-\alpha^2 x^2}}{\sqrt{\pi} x^2} - 3l^2 \left[ \frac{\operatorname{erfc}(\alpha x)}{x^5} + \frac{2\alpha (3 + 2\alpha^2 x^2) e^{-\alpha^2 x^2}}{3\sqrt{\pi} x^4} \right]. \quad (9c)$$

For the configurations of Fig. 1, the complex Hermitian matrix  $\mathbf{M}_D(\mathbf{q})$  of Eq. (7) can be transformed into a real and symmetric matrix. This is achieved by first applying the unitary transformation  $\bar{\mathbf{M}}_D(\mathbf{q}) = \mathbf{U} \mathbf{M}_D(\mathbf{q}) \mathbf{U}^\dagger$ , with  $\mathbf{U}$  a  $4 \times 4$  matrix defined as

$$\mathbf{U} = \frac{1}{\sqrt{2}} \begin{pmatrix} \mathbf{I}_2 & i\mathbf{I}_2 \\ i\mathbf{I}_2 & \mathbf{I}_2 \end{pmatrix}, \quad (10)$$

with  $\mathbf{I}_2$  the  $2 \times 2$  identity matrix. This transformation brings the dynamical matrix into the symmetric form

$$\bar{\mathbf{M}}_D(\mathbf{q}) = \begin{pmatrix} \mathbf{M}_{++} + \operatorname{Im}[\mathbf{M}_{+-}] & \operatorname{Re}[\mathbf{M}_{+-}] \\ \operatorname{Re}[\mathbf{M}_{+-}] & \mathbf{M}_{++} - \operatorname{Im}[\mathbf{M}_{+-}] \end{pmatrix}, \quad (11a)$$

$$\text{with } \mathbf{M}_{+\sigma} \equiv \begin{pmatrix} M_{+\sigma}^{xx} & M_{+\sigma}^{xy} \\ M_{+\sigma}^{xy} & M_{+\sigma}^{yy} \end{pmatrix}. \quad (11b)$$

That the matrix  $\bar{\mathbf{M}}_D(\mathbf{q})$  is real now stems from the fact that  $\operatorname{Im}[\mathbf{M}_{+-}]$  vanishes for a lattice with inversion symmetry<sup>46,48</sup>, which is the case for all lattice configurations considered in this work.

For each quasi-momentum  $\mathbf{q}$ , diagonalizing  $\bar{\mathbf{M}}_D(\mathbf{q})$  provides the square of the phonon frequencies,  $\omega_\alpha(\mathbf{q})^2$  (with  $1 \leq \alpha \leq 4$ ), which correspond to the four distinct phonon modes of the bilayer system. Within the harmonic approximation, the stability of the various lattice configurations is linked to the sign of the eigenvalues of  $\bar{\mathbf{M}}_D(\mathbf{q})$ . That is, a lattice configuration is stable if all four eigenvalues of  $\bar{\mathbf{M}}_D(\mathbf{q})$  are positive for all quasi-momenta  $\mathbf{q}$ , i.e.  $\omega_\alpha(\mathbf{q})^2 > 0$ , while it is unstable if one (or more) of the four eigenvalues is negative for a given quasi-momentum  $\mathbf{q}$ , c.f.  $\omega_\alpha(\mathbf{q})^2 < 0$ .

### A. Ground state configuration

In this subsection we calculate the phonon spectrum for the ground-state configuration MH as a function of the inter-layer separation  $\xi$ , using the techniques described above. As expected, we find both acoustic and optical modes, with the latter related to out-of-phase

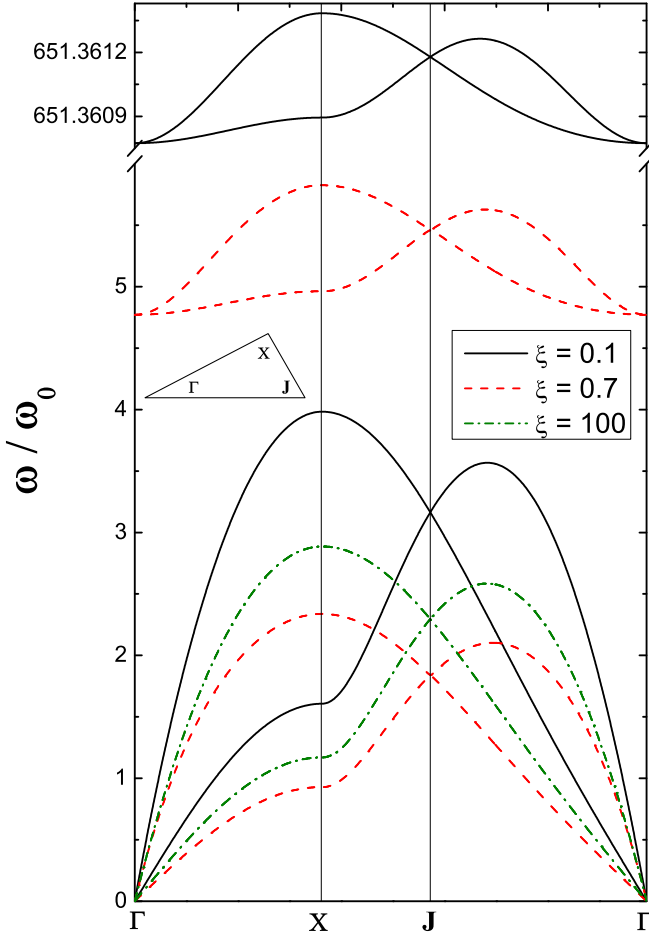


FIG. 4: (Color online) Phonon dispersion curves  $\omega_{\alpha}(\mathbf{q})$  for the MH lattice configuration in units of  $\omega_0 = \sqrt{d^2 n^{5/2}/m}$ , for  $\xi = 0.1$  (solid lines),  $\xi = 0.7$  (dashed lines) and  $\xi \rightarrow \infty$  (dash-dotted lines). The frequencies are presented along the high symmetry directions in the Brillouin zone. The high-symmetry points  $\Gamma$ , X and J are depicted in the inset. Note that the different axis scaling for the high-frequency regime  $\omega \gg 6\omega_0$ .

vibrations of particles in different layers. We show that the longitudinal and transverse sound velocities of the acoustic modes show a non-monotonic dependence on  $\xi$ , which is linked to the anisotropic nature of the dipole-dipole interaction. The picture emerging from these studies is one where the bilayer structure behaves for vanishing inter-layer separations  $\xi \ll 1$  as a single 2D crystal of particles with double mass and double dipole-moment, while for  $\xi \gg 1$  the two layers behave as independent 2D crystals. Within the harmonic approximation inherent to the present discussion, the transition between these two situations occurs approximately for inter-layer distances such that the nearest-neighbor inter-layer interaction switches from repulsive ( $\xi \ll 1$ ) to attractive ( $\xi \gg 1$ ).

Figure 4 shows the phonon dispersion relations for the

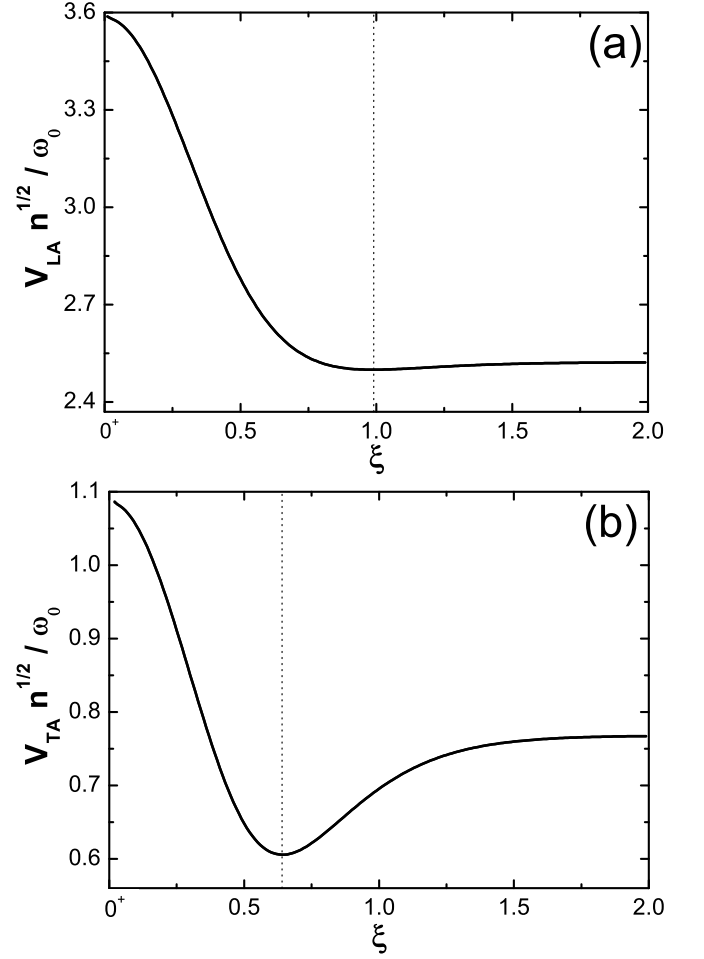


FIG. 5: (Color online) Sound velocities for the MH lattice configuration as a function of the dimensionless layer separation  $\xi$ : (a) Longitudinal sound velocity  $v_{LA}$  and (b) transverse sound velocity  $v_{TA}$ , in units of  $\omega_0/\sqrt{n}$ .

MH lattice configuration along the high symmetry directions in the Brillouin zone for a three values of  $\xi$ , i.e.  $\xi = 0.1, 0.7, 100$  (solid, dashed, dash-dotted lines). The frequencies are in units of the characteristic phonon frequency  $\omega_0 = \sqrt{d^2 n^{5/2}/m}$ . The symmetry points  $\Gamma$ , X and J are depicted in the inset. The figure shows that for  $\xi \rightarrow \infty$  there are two phonon branches. Each one of these branches is doubly degenerate, corresponding to independent longitudinal and transverse acoustic phonon modes of the two layers. We find that, as expected, the modes exactly match those of a single layer, confirming that in the limit  $\xi \rightarrow \infty$  the two layers behave as independent. For finite  $\xi$  the dipole-dipole interaction couples the two layers, and lattice vibrations in the two layers become correlated. Accordingly, the figure shows that for  $\xi = 0.7$  (dashed lines) and  $\xi = 0.1$  (solid lines) the phonon modes develop separate acoustic and optical branches. Since the MH lattice structure can be represented as the repetition of a basis cell comprising two particles, one per layer, stacked on top of each other,

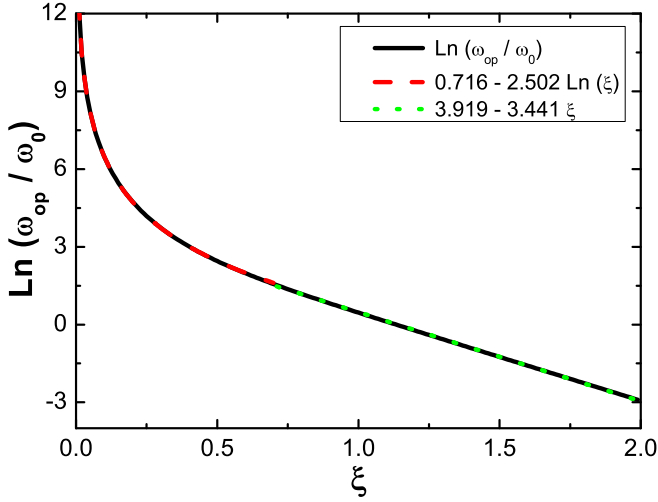


FIG. 6: (Color online) Optical frequencies  $\omega_{\text{op}}$  (in logarithmic scale in units of  $\omega_0$ ) at the  $\Gamma$  point for the MH lattice configuration as a function of  $\xi$  (solid line), along with the approximations  $\ln(\omega_{\text{op}}/\omega_0) \approx 0.716 - 2.502 \ln \xi$  for  $\xi \lesssim 0.7$  (dashed line) and  $\ln(\omega_{\text{op}}/\omega_0) \approx 3.919 - 3.441\xi$  for  $\xi \gtrsim 0.7$  (dotted line).

the optical modes are easily understood as arising from out-of-phase vibrations of the dipoles in each basis cell. The figure shows that the optical frequency of vibration increases with decreasing inter-layer distance, and the bandwidth of the optical branch tends to shrink (note that in the figure the scales for the optical modes for  $\xi = 0.7$  and  $\xi = 0.1$  are different). In the (unphysical) limit  $\xi \rightarrow 0$ , the phonon spectrum reduces to one where there is only one, i.e. *non-degenerate*, longitudinal acoustic and one transverse acoustic mode, while the optical branches are shifted to infinitely large frequencies. This observation is consistent with the system behaving as a single layer of dipoles with double mass and double dipole strength, arranged in a hexagonal configuration (see below).

Figure 4 shows that the acoustic branches for  $\xi = 0.7$  have lower frequencies than the corresponding branches for  $\xi = 0.1$  and  $\xi \rightarrow \infty$ , indicating a non-monotonic dependence of the frequencies on  $\xi$ . In order to better investigate this point, in Fig. 5(a) and Fig. 5(b) we plot the longitudinal and transverse sound velocities  $v_{\text{LA}} = \partial\omega_{\text{LA}}/\partial q|_{q=0}$ ,  $v_{\text{TA}} = \partial\omega_{\text{TA}}/\partial q|_{q=0}$ , with  $\omega_{\text{LA}}$  and  $\omega_{\text{TA}}$  the frequencies of the longitudinal and transverse acoustic modes, respectively. We find that for  $\xi \gg 1$ , the longitudinal and transverse sound velocities tend to  $v_{\text{LA}} \simeq 2.544\omega_0/\sqrt{n}$  and  $v_{\text{TA}} \simeq 0.768\omega_0/\sqrt{n}$ , respectively. These values correspond to the sound velocities of a monolayer hexagonal lattice configuration, consistent with the observation above that for  $\xi \gg 1$  the crystal vibrations in the two layers become independent. In the opposite limit  $\xi \rightarrow 0$ , we find that the sound velocities are larger than those above *exactly* by a factor  $\sqrt{2}$ . A simple comparison with the characteristic phonon

frequency  $\omega_0 = \sqrt{d^2 n^{5/2}/m}$  shows that this  $\sqrt{2}$ -factor is consistent with the system behaving as a single layer of dipoles of mass  $2m$  and dipole strength  $2d$ .

Figure 5 shows that the dependence of the sound velocities on  $\xi$  is non-monotonic. In particular, minima for  $v_{\text{LA}}$  and  $v_{\text{TA}}$  occur at  $\xi = \xi_0 \approx 1$  and  $0.64$ , respectively (see Appendix B). This non-monotonic behavior is linked to the anisotropic character of the dipole-dipole interaction. In fact, for  $\xi \rightarrow \infty$  the two layers behave as independent hexagonal crystals. For finite  $\xi$ , the inter-layer interactions couple the two layers. This coupling, which is responsible for the formation of the optical band, splits the degeneracy of the phonon frequencies, lowering the acoustic sound velocity, which is associated with a softening of the crystal, see Fig. 4. For  $\xi \lesssim 1$  the optical and acoustic branches are well separated, corresponding to the formation of a crystal of tightly bound pairs of dipoles. For  $\xi \rightarrow 0$  the sound velocity is a  $\sqrt{2}$  larger than at  $\xi \rightarrow \infty$ , as discussed above, and this determines the appearance of a minimum in between, and we observe that the value  $\xi \approx 1$  roughly corresponds to the inter-layer distance at which the interaction of a dipole at  $\mathbf{R}_{+,j}$  with next-nearest-neighbor in the opposite layer at position  $\mathbf{R}_{-,j'}$  switches from attractive to repulsive. We remark that although the crystalline structure is softened for finite  $\xi$ , the sound velocity remains always finite. This is due to the anisotropic character of the dipole-dipole interactions, which ensures that the MH configuration is *always* the *stable* ground-state configuration.

Figure 6 shows as a solid line the optical frequencies  $\omega_{\text{op}}$  as a function of  $\xi$  in logarithmic scale at the  $\Gamma$  point, where the two optical frequencies are degenerate. We notice that for  $\xi \gtrsim 0.7$  the frequencies decay exponentially with increasing  $\xi$  as  $\ln(\omega_{\text{op}}/\omega_0) \approx 3.919 - 3.441\xi$  (c.f. dotted line), while they diverge as a power law  $\ln(\omega_{\text{op}}/\omega_0) \approx 0.716 - 2.502 \ln(\xi)$  for  $\xi \lesssim 0.7$  (c.f. dashed line). This change in behavior is another manifestation of the crossover from two independent layers to a single crystal of paired dipoles.

## B. Excited-state configurations

In this subsection we study the *meta*-stability of the excited-state configurations OCH, ZS and ZR introduced in Sect. II, by calculating the phonon modes for each configuration. For a given interlayer distance  $\xi$ , within the applicability of the harmonic approximation, regions of meta-stability and instability for the above configurations correspond to real and imaginary values of the computed phonon frequencies, respectively. By analyzing the sound velocities of the phonon excitations, we find that the instability of the OCH and ZS crystalline structures is associated with the vanishing of the transverse acoustic branch of the phonon modes in the directions  $\Gamma X$  and  $\Gamma M$ . We thus derive a stability diagram for the low-lying excitations of the system as a function of  $\xi$ , see below. This is interesting, since

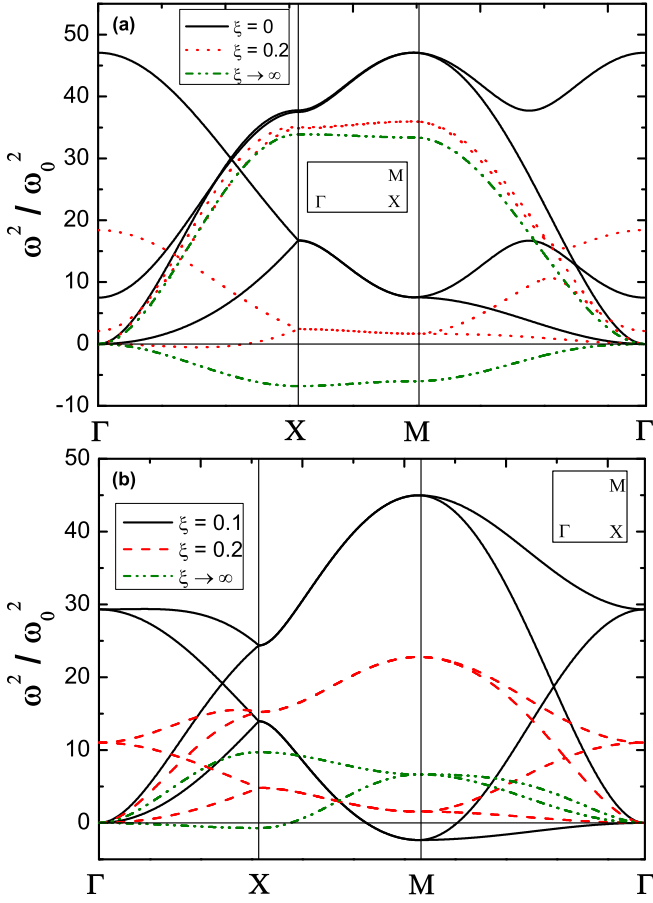


FIG. 7: (Color online) Square of the phonon frequencies  $\omega_\alpha^2$  in units of  $\omega_0^2 = d^2 n^{5/2}/m$  (a) for the OCH configuration at  $\xi = 0$  (solid lines),  $\xi = 0.2$  (dashed lines) and  $\xi \rightarrow \infty$  (dash-dotted lines) and (b) for the ZS configurations at  $\xi = 0.1$  (solid lines),  $\xi = 0.2$  (dashed lines) and  $\xi \rightarrow \infty$  (dash-dotted lines). The frequencies are shown along the high symmetry directions in reciprocal space for each lattice configuration. The high-symmetry points  $\Gamma$ , X and M are depicted in the insets.

in principle these excited-state configurations may be realized, e.g. by first trapping cold polar molecules in optical lattices with the same geometry as OCH and ZS crystals, increasing the dipole-dipole interactions using external fields, forming interaction-induced OCH and ZS crystals, and finally adiabatically removing the lattice potential.

Panels (a) and (b) in Fig. 7 show the square of the phonon frequencies for the OCH and ZS lattice configurations, respectively, for a few values of  $\xi$  and in units of  $\omega_0^2 = d^2 n^{5/2}/m$ . The phonon spectra in Fig. 7 are shown along the high symmetry directions in reciprocal space, with symmetry points labeled in the insets. The figure shows that for certain values of  $\xi$  the square of the phonon frequencies becomes negative,  $\omega^2 < 0$ , signaling an instability of the corresponding crystalline structure for the given value of  $\xi$ . In panels

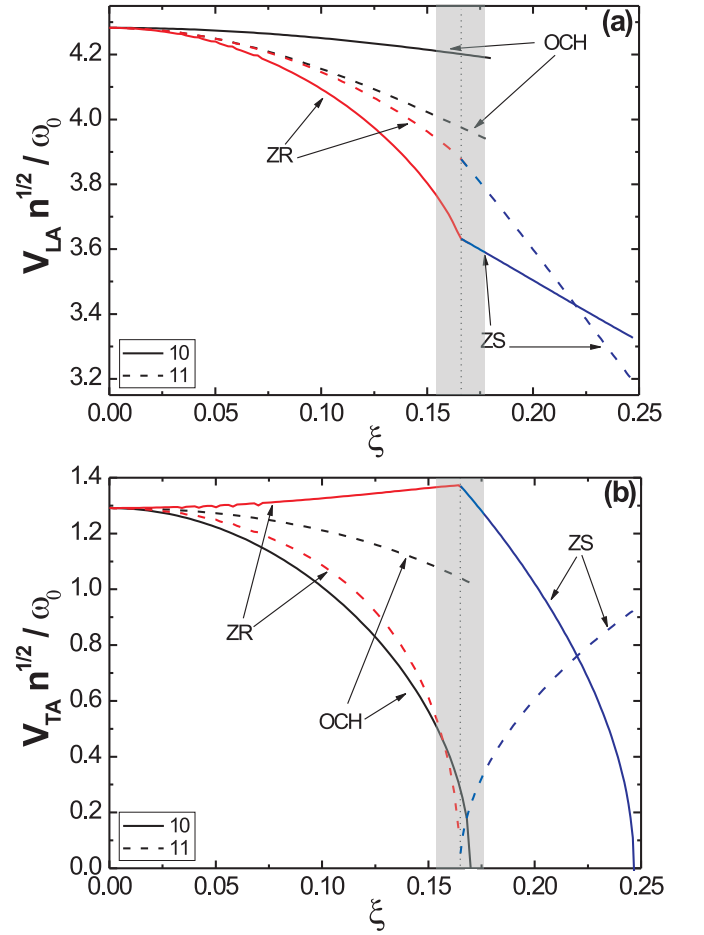


FIG. 8: (Color online) (a) Longitudinal sound velocities  $v_{LA}$  and (b) transverse sound velocities  $v_{TA}$  in units of  $\omega_0/\sqrt{n}$  along the (1,0) (solid lines) and the (1,1) (dotted lines) directions for OCH, ZR and ZS lattice configurations. The vertical dotted line denotes the boundary between ZR and ZS. The gray shading corresponds to the transition region where the harmonic approximation for the phonon excitations may become inadequate.

(a) and (b), regions of meta-stability are present for  $\xi = 0$  and  $\xi = 0.2$ , respectively. In fact, we determined numerically that the OCH configuration of panel (a) is *meta-stable* for  $\xi \lesssim 0.170$ , while the ZS configuration of panel (b) is *meta-stable* in the range  $0.166 \lesssim \xi \lesssim 0.247$ . We notice that in these regimes where  $\omega^2 > 0$  the system in the OCH and ZS configurations is *meta-stable*, since the associated crystalline structures are excited states of the system. By analyzing the sound velocities of the phonon excitations, we found that the instability of the OCH and ZS crystalline structures is associated with the vanishing of the transverse acoustic branch of the phonon modes in the directions (1,1) and (1,0), as detailed below.

Panels (a) and (b) in Fig. 8 show the sound velocities of the transverse acoustic (TA) and longitudinal acous-



tic (LA) modes for the OCH, ZS and ZR configurations as functions of  $\xi$  in the range of stability of each configuration, respectively. In the figure, the continuous and dashed lines correspond to the (1,0) and (1,1) directions, respectively. Panel (a) shows that the TA mode for the OCH configuration vanishes in the (1,0) direction at  $\xi \simeq 0.170$  [see also Fig. 7(a)]. The TA mode for the ZS configuration vanishes in the (1,1) and (1,0) directions for  $\xi \lesssim 0.166$  and  $\xi \gtrsim 0.25$ , respectively. In addition, panel (b) shows that the longitudinal modes for all three configurations soften with increasing  $\xi$ . The transverse and longitudinal sound velocities for the ZR configuration interpolate between those of the OCH and ZS configurations, see Fig. 8(a) and Fig. 8(b), coinciding with those at  $\xi = 0$  and  $\xi \approx 0.166$ , respectively.

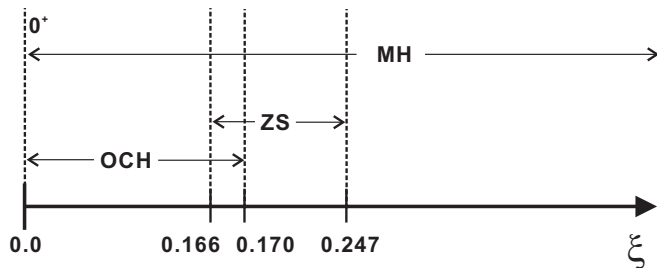


FIG. 9: Approximate regions of stability for the MH, ZS, and OCH configurations, as a function of  $\xi$ .

Figure 9 summarizes the regions of stability for the MH configuration, which is the ground-state for any  $\xi > 0$ , the OCH and the ZS configurations. We remark that the values  $\xi = 0.166$ ,  $0.170$  and  $0.247$  have been obtained numerically, in the harmonic approximation for the phonon spectrum. Since the harmonic approximation is bound to break down around any transition points between various configurations, the numerical values  $0.166$  and  $0.170$  should be taken with caution, and simply interpreted as *indicative* of the transition region.

For completeness, in Fig. 10 we show the optical frequencies at the  $\Gamma$  point as function of  $\xi$  for the OCH, ZR and ZS lattice configurations. As expected, we find that the frequencies corresponding to the ZR configuration interpolate between those of the OCH and ZS configurations. In particular, they become degenerate around  $\xi \approx 0.170$ , where the ZS configuration becomes stable. This degeneracy is a natural consequence of the fact that the aspect ratio  $a_2/a_1$  of the ZS configuration is 1. We notice that the different behaviors of the optical frequencies may be used to distinguish experimentally the various metastable structures, when initially prepared in tailored optical lattice potentials, as discussed at the beginning of this subsection.

#### IV. CLASSICAL MELTING

In this section we discuss the classical melting temperature of the bilayer system, as obtained in the har-

monic approximation for the excitations of the crystal using a (modified) Lindemann criterion. The latter states that for a given configuration the melting occurs when the *mean relative displacement* between neighboring sites becomes of the order of the mean interparticle distance  $r_0 = 1/\sqrt{\pi n}$  (see Table. I for the configurations of Fig. 1)<sup>49</sup>. This reads

$$\frac{\sqrt{\langle |\mathbf{u}(\mathbf{R}) - \mathbf{u}(\mathbf{R} + \mathbf{r})|^2 \rangle}}{r_0} = \delta_m, \quad (12)$$

where  $\langle |\mathbf{u}(\mathbf{R}) - \mathbf{u}(\mathbf{R} + \mathbf{r})|^2 \rangle$  is the relative mean square displacement,  $\mathbf{u}(\mathbf{R})$  and  $\mathbf{u}(\mathbf{R} + \mathbf{r})$  are the displacement vectors at site  $\mathbf{R}$  and at its nearest neighbor site  $\mathbf{R} + \mathbf{r}$ ,  $\langle \rangle$  is a thermal average, and  $\delta_m < 1$  is a parameter which in general has to be determined numerically.

The left-hand side of Eq. (12) is computed in the harmonic approximation for the phonons as follows. Each particle in the bilayer structure has two different kinds of nearest-neighbors: in-plane and out-of-plane. Thus, in analogy to the Coulomb case of Ref.<sup>46</sup> we define the *intralayer* ( $\Delta u_{++}$ ) and *interlayer* ( $\Delta u_{+-}$ ) correlation func-

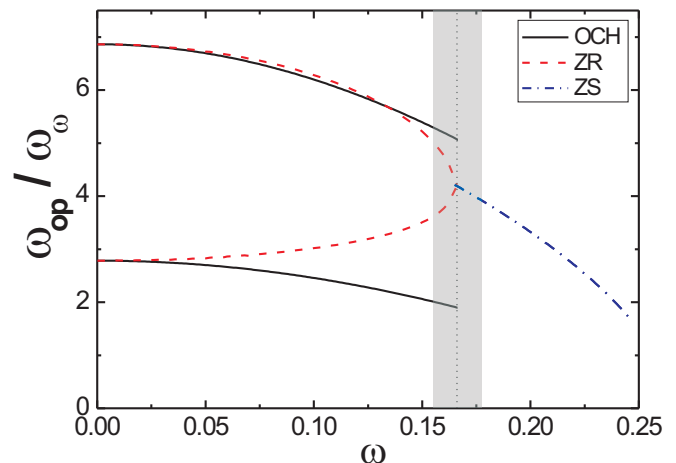


FIG. 10: (Color online) Optical frequencies  $\omega_{\text{op}}$  in unit of  $\omega_0$  at the  $\Gamma$  point for the OCH, ZR and ZS lattice configurations. The vertical dotted line denotes the boundary between ZR and ZS. The gray shading corresponds to the transition region where the harmonic approximation for the phonon excitations may become inadequate.

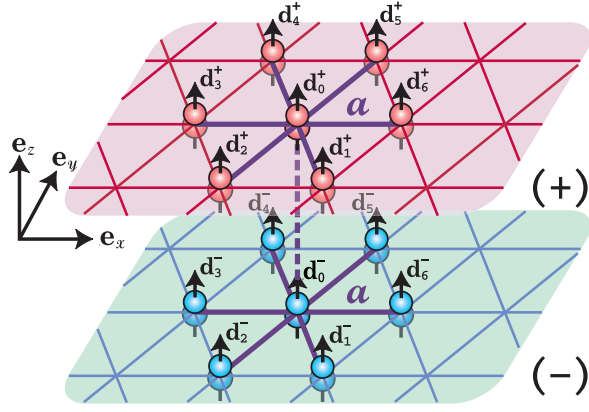


FIG. 11: (Color online) Illustration of the dipole-configuration for the MH structure leading to the modified Lindemann criterion.

tions (see Appendix C)

$$\begin{aligned} \Delta u_{++} &= \frac{1}{S_+} \sum_{\gamma=x,y} \sum_{h=1 \dots S_+} \langle |u_\gamma^+(0) - u_\gamma^+(h)|^2 \rangle \\ &= \frac{2k_B T}{N S_+ m} \sum_{\mathbf{q}, j} \frac{1}{\omega^2(\mathbf{q}, j)} \left\{ [\rho_x^+(\mathbf{q}, j)^2 + \rho_y^+(\mathbf{q}, j)^2] \right. \\ &\quad \left. [1 - \cos(\mathbf{q} \cdot \mathbf{R}_h^+)] \right\}, \end{aligned} \quad (13a)$$

$$\begin{aligned} \Delta u_{+-} &= \frac{1}{S_-} \sum_{\gamma=x,y} \sum_{h=1 \dots S_-} \langle |u_\gamma^+(0) - u_\gamma^-(h)|^2 \rangle \\ &= \frac{k_B T}{N S_- m} \sum_{\mathbf{q}, j} \frac{1}{\omega^2(\mathbf{q}, j)} \left\{ [\rho_x^+(\mathbf{q}, j)^2 + \rho_x^-(\mathbf{q}, j)^2 \right. \\ &\quad \left. + \rho_y^+(\mathbf{q}, j)^2 + \rho_y^-(\mathbf{q}, j)^2] - 2 [\rho_x^+(\mathbf{q}, j) \rho_x^-(\mathbf{q}, j) \right. \\ &\quad \left. + \rho_y^+(\mathbf{q}, j) \rho_y^-(\mathbf{q}, j)] \cos(\mathbf{q} \cdot \mathbf{R}_h^-) \right\}. \end{aligned} \quad (13b)$$

Here  $S_\sigma$  is the number of nearest-neighbor dipoles in layer  $\sigma = \pm$ ,  $u_\gamma^\sigma(h)$  is the  $\gamma^{\text{th}}$  component of the displacement of a particle at position  $h$  in the layer  $\sigma$ ,  $\rho_\gamma^\sigma(\mathbf{q}, j)$  is the  $\gamma^{\text{th}}$  component of the eigenvector of the  $j^{\text{th}}$  mode at point  $\mathbf{q}$  in the Brillouin zone of the sublattice in layer  $\sigma$ , and  $\mathbf{R}_h^\tau$  is the relative vector connecting one particle to its  $h^{\text{th}}$  nearest-neighbor in the same ( $\tau = +$ ) or opposite ( $\tau = -$ ) layers. We notice that the number of nearest-neighbors  $S_\sigma$  and their distance depends on the considered lattice configuration (see Fig. 1) and  $\xi$ . In particular, Fig. 11 shows that, in the relevant case of the groundstate configuration MH (see Sect. IV A below), the number of *in-plane* nearest-neighbors is 6, while that of *out-of-plane* nearest-neighbors is 7.

The correlation  $\langle [\mathbf{u}(\mathbf{R}) - \mathbf{u}(\mathbf{R} + \mathbf{r})]^2 \rangle$  of Eq. (12) is now computed as

$$\langle [\mathbf{u}(\mathbf{R}) - \mathbf{u}(\mathbf{R} + \mathbf{r})]^2 \rangle = \Delta u_{++} + f(l) \Delta u_{+-}, \quad (14)$$

where the function  $f(l)$  describes the influence of lattice vibrations in one layer on the lattice vibrations in the opposite layer, and it is defined as

$$f(l) = \frac{1}{(1 + \kappa l^2)^{5/2}} + \frac{-3\kappa l^2}{(1 + \kappa l^2)^{7/2}}. \quad (15)$$

Here, the geometric parameter  $\kappa$  can be obtained from Table I, and it reads  $\kappa = (a^2)^{-1}$  and  $\kappa = (|\mathbf{c}|^2)^{-1}$  for the MH and zigzag lattice configurations, respectively. This expression for  $f(l)$  is chosen to be proportional to the in-plane part of the force between two nearest-neighbor dipoles in opposite layers and it satisfies the conditions

$$\lim_{l \rightarrow 0} f(l) = 1 \quad \text{and} \quad \lim_{l \rightarrow \infty} f(l) = 0,$$

where the latter condition is due to the fact that vibrations in the two layers are independent for infinite inter-layer separations.

#### A. Melting of the ground state configuration

In this subsection we determine the classical melting temperature  $T_m$  of the ground-state crystal configuration MH as a function of  $\xi$ , using the modified Lindemann criterion introduced above. We find a non-monotonic dependence of  $T_m$  on  $\xi$ , which we attribute to the anisotropic nature of the dipole-dipole interactions. This is interesting since for certain temperatures it is associated with a *re-entrant* melting behavior in the form of *solid-liquid-solid-liquid* transitions.

Figure 12 shows the melting temperature  $T_m$  as a function of  $\xi$ , as calculated from the Lindemann criterion with  $\delta_m = 0.23$  within the harmonic approximation for the phonon modes. The precise value of  $\delta_m$  should in principle be obtained numerically, e.g. using molecular dynamics simulations. In the absence of such a computation for a classical bilayer crystal, the value of  $\delta_m = 0.23$  has been chosen in analogy to the one obtained in Ref.<sup>30</sup> for the *quantum* melting transition from a single-layer crystal of bosonic dipoles into a superfluid using Diffusion Monte-Carlo techniques. Using this value of  $\delta_m$  in Eq. (12), we find that for  $\xi \gg 1$  the classical melting temperature of the bilayer crystal tends to the value  $T_0 \approx 0.066d^2/a^3$ . By construction, the latter corresponds to the classical melting temperature of a single hexagonal crystal as computed in the harmonic approximation discussed above. We here notice that the obtained value of  $T_0$  is of the order of the actual one  $T_0^{\text{num}} \approx 0.089d^2/a^3$  for a classical single-layer crystal, as obtained numerically by molecular dynamics simulations<sup>50</sup>. Since the spirit of the Lindemann criterion is that of a *qualitative* estimate of the transition point, in the following we will be content with the value  $T_0$ .

For  $\xi \ll 1$  the figure shows that the melting temperature tends to  $T_m = 4T_0$ . This is consistent with the picture of a hexagonal crystal made of paired dipoles with

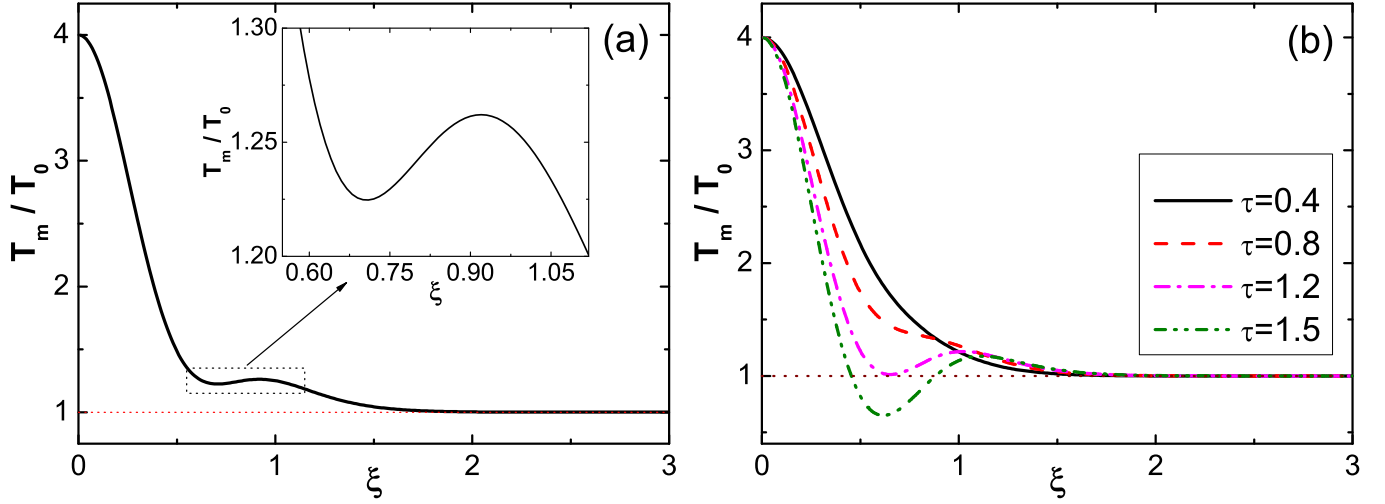


FIG. 12: (Color online) (a) Melting temperature  $T_m$  as a function of  $\xi$  for the MH lattice configuration (solid line). The unit  $T_0 \approx 0.066d^2/a^3$  corresponds to the melting temperature of a single-layer crystal, as computed from Eq. (12) with  $\delta_m = 0.23$ . The dashed line is a guide to the eye. (b) Melting temperature  $T_m$  as a function of  $\xi$  for particles interacting via the potential  $V_{ij}^{\text{int}}$  of Eq. (16). Here,  $\tau$  is the strength of the attractive part of the potential (see text), with  $\tau = 1$  corresponding to the dipole-dipole interaction of panel (a). The dotted line is a guide to the eye.

dipole strength  $d^* = 2d$ , as discussed in Sect. III A. Interestingly, the figure shows that  $T_m$  has a non-monotonic dependence on  $\xi$  around  $\xi \approx 1$ . In particular, the  $T_m$ -vs- $\xi$  curve has a local maximum and a local minimum at  $\xi \approx 1$  and  $\xi \approx 0.6$ , respectively. As noticed in Sect. III A, this region of  $\xi$ -values corresponds to the distance at which the dipole-dipole interaction between a particle in one layer and its nearest-neighbor in the opposite layer changes sign from attractive to repulsive (e.g.  $d_0^-$  and  $d_j^+$  in Fig. 1, respectively, with  $1 \leq j \leq 6$ ).

In order to check that the non-monotonicity is in fact connected with the anisotropic nature of the dipole-dipole interaction, in Fig 12(b) we have plotted the melting temperature for an *artificial* system of particles where the strength of the attractive part of the dipole-dipole interaction can be tuned, and thus the particles interact via a potential of the form

$$V_{ij}^{\text{int}} = d^2 \left( \frac{1}{|\mathbf{r}_{ij}|^3} + \tau \frac{-3 l^2}{|\mathbf{r}_{ij}|^5} \right), \quad (16)$$

with  $\tau$  a constant,  $0 \leq \tau < \infty$ , and  $|\mathbf{r}_{ij}|$  the interparticle distance. We find that the non-monotonic character of the curve is enhanced for  $\tau > 1$ , while it tends to disappear for  $\tau < 1$  and in particular it vanishes for  $\tau \lesssim 0.9$ . In the limit  $\tau \rightarrow 0$  of purely repulsive interactions (not shown) the system resembles the Coulomb case of Ref. 46, and accordingly we find that the MH lattice ceases to be the groundstate configuration.

The observations above confirm that the reentrant (non-monotonic) behavior of  $T_m$  as a function of  $\xi$  is due to the attractive character of the dipole-dipole interactions. This indicates that it is possible to alternate solid and liquid phases by changing the interlayer distance or

the density of the molecules.

## V. CONCLUSION

In this work we studied the structure, the stability and the melting of a classical bilayer system of dipoles, polarized perpendicular to the layers, as a function of the interlayer distance and the density of dipoles in each layer. Using the Ewald summation technique, we have computed the ground-state energy and the phononic spectrum of a few physically-motivated lattice configurations, finding that the ground state is always the matching hexagonal crystal configuration, where two triangular lattices are stacked on top of each other, as expected. Higher-energy configurations have been found to be metastable in different regimes of interlayer distances and dipole densities. These configurations may be realized using polar molecules trapped in optical lattices of properly chosen geometry.

The main result of this work is that the anisotropic nature of the dipole-dipole interaction potential profoundly affects the dynamical properties of the bilayer system of dipoles, and its melting behavior. In fact, on one hand we found that the attractive part of the potential determines a non-monotonic dependence on  $\xi$  of the longitudinal and transverse sound velocities in the ground-state configuration. On the other hand, we have shown that the classical melting temperature of the bilayer crystal has an interesting reentrant behavior as a function of  $\xi$ . This reentrant behavior is due to the anisotropy of the dipole-dipole interaction, and it entails that it is possible to alternate various crystalline and liquid phases by

changing  $\xi$  at a fixed temperature.

The present analysis is motivated by the recent developments in the physics of cold molecular gases, which may provide for a physical realization of these systems. In particular, the classical melting of the bilayer crystalline phases may be realized in future in setups where cold polar molecules are trapped in adjacent wells of a one-dimensional optical lattice, and their dipoles are polarized by a static electric field oriented parallel to the optical lattice. Under appropriate trapping conditions<sup>12,29</sup>, the resulting *in-plane* dipole-dipole interactions are purely repulsive, while inter-plane interactions can be repulsive or attractive.

### Acknowledgments

The authors thank P. Zoller for stimulating discussions. Lu acknowledges a supporting scholarship by Eurasia-Pacific Uninet and the kind hospitality provided by the University of Innsbruck and IQOQI of the Austrian Academy of Sciences. This work is supported by the the National Natural Science Foundation of China, the European Union project OLAQUI (FP6-013501-OLAQUI) and the Austrian Science Foundation (FWF).

### APPENDIX A: RAPIDLY CONVERGENT FORM OF $\psi_0$ AND $\psi_I$

The direct numerical computation of sums over lattice sites with long-range dipole-dipole interactions is in general impractical. Thus in the following we transform each sum into rapidly convergent forms using Ewald method.<sup>46,51</sup> The detailed techniques are shown in the following. For the calculation of the rapidly convergent form of the energy, at first we define the following two functions

$$\psi_0(\mathbf{r}, \mathbf{q}) = e^{i\mathbf{q}\cdot\mathbf{r}} \sum_{j \neq 0} \frac{e^{-i\mathbf{q}\cdot(\mathbf{R}_j+\mathbf{r})}}{|\mathbf{R}_j+\mathbf{r}|^3}, \quad (\text{A1a})$$

$$\begin{aligned} \psi_I(\mathbf{r}, \mathbf{q}) &= e^{i\mathbf{q}\cdot\mathbf{r}} \sum_j \left( \frac{e^{i\mathbf{q}\cdot(\mathbf{R}_j+\mathbf{c}+\mathbf{r})}}{|\tilde{\mathbf{R}}_j+\mathbf{r}|^3} \right. \\ &\quad \left. + \frac{-3 l^2 e^{i\mathbf{q}\cdot(\mathbf{R}_j+\mathbf{c}+\mathbf{r})}}{|\tilde{\mathbf{R}}_j+\mathbf{r}|^5} \right) \\ &= \psi_{I1} - 3 l^2 \psi_{I2}, \end{aligned} \quad (\text{A1b})$$

where

$$\psi_{I1} = \sum_j \frac{e^{i\mathbf{q}\cdot(\mathbf{R}_j+\mathbf{c}+\mathbf{r})}}{|\tilde{\mathbf{R}}_j+\mathbf{r}|^3}, \quad (\text{A2a})$$

$$\psi_{I2} = \sum_j \frac{e^{i\mathbf{q}\cdot(\mathbf{R}_j+\mathbf{c}+\mathbf{r})}}{|\tilde{\mathbf{R}}_j+\mathbf{r}|^5}, \quad (\text{A2b})$$

with  $\mathbf{R}_j \equiv \mathbf{R}_{\sigma,j} - \mathbf{R}_{\sigma,0}$  and  $|\tilde{\mathbf{R}}_j+\mathbf{r}| \equiv (|\mathbf{R}_j+\mathbf{c}+\mathbf{r}|^2 + l^2)^{1/2}$ . Then  $E_0$  and  $E_I$  can be obtained from

$$E_0 = \lim_{\mathbf{r} \rightarrow 0} d^2 \psi_0(\mathbf{r}, 0), \quad (\text{A3a})$$

$$E_I = \lim_{\mathbf{r} \rightarrow 0} d^2 \psi_I(\mathbf{r}, 0). \quad (\text{A3b})$$

We use the identity based on the integral representation of the gamma function

$$\frac{1}{x^{2s}} = \frac{1}{\Gamma(s)} \int_0^\infty t^{s-1} \exp(-x^2 t) dt, \quad (\text{A4})$$

with  $s = 3/2$ ,  $\Gamma(3/2) = \sqrt{\pi}/2$  for  $\psi_0$  and  $\psi_{I1}$ ,  $s = 5/2$ ,  $\Gamma(5/2) = 3\sqrt{\pi}/4$  for  $\psi_{I2}$ , and the 2D Poisson summation formula

$$\begin{aligned} &\sum_j \exp(-|\rho + \mathbf{R}_j|^2 t - i\mathbf{q} \cdot (\rho + \mathbf{R}_j)) \\ &= \frac{\pi}{L^2} t^{-1} \sum_j \exp(i\mathbf{G}_j \cdot \rho) \exp\left(-\frac{|\mathbf{G}_j + \mathbf{q}|^2}{4t}\right) \end{aligned} \quad (\text{A5})$$

where  $\mathbf{G}_j = j_1 \mathbf{b}_1 + j_2 \mathbf{b}_2$  (with integers  $i, j$ ) is the two-dimensional vector in reciprocal lattice,  $L^2 = 1/n$  is the area per primitive cell. Then  $\psi_0(\mathbf{r}, \mathbf{q})$  can be expressed by

$$\begin{aligned} \psi_0(\mathbf{r}, \mathbf{q}) &= \frac{\pi}{L^2} \sum_j e^{i(\mathbf{q}+\mathbf{G}_j)\cdot\mathbf{r}} \frac{2}{\sqrt{\pi}} \int_0^{\alpha^2} t^{-1/2} \\ &\quad \exp\left(-\frac{|\mathbf{G}_j + \mathbf{q}|^2}{4t}\right) dt - \frac{2}{\sqrt{\pi}} \int_0^{\alpha^2} t^{1/2} e^{-|\mathbf{r}|^2 t} dt \\ &\quad + \sum_{j \neq 0} e^{-i\mathbf{q}\cdot\mathbf{R}_j} \frac{2}{\sqrt{\pi}} \int_{\alpha^2}^\infty t^{1/2} e^{-|\mathbf{R}_j+\mathbf{r}|^2 t} dt, \end{aligned} \quad (\text{A6})$$

where  $\alpha$  is a small positive number. After using the integration

$$\begin{aligned} &\int_{\alpha^2}^\infty t^{1/2} \exp(-|x|^2 t) dt \\ &= \frac{\sqrt{\pi}}{2|x|^3} \operatorname{erfc}(\alpha|x|) + \frac{\alpha \exp(-\alpha^2|x|^2)}{|x|^2}, \end{aligned} \quad (\text{A7})$$

and

$$\begin{aligned} &\int_0^{\alpha^2} t^{-1/2} \exp\left(-\frac{|x|^2}{4t}\right) dt \\ &= \exp\left(-\frac{|x|^2}{4\alpha^2}\right) \left\{ 2\alpha - \exp\left(\frac{|x|^2}{4\alpha^2}\right) \right. \\ &\quad \left. \times |x| \sqrt{\pi} \operatorname{erfc}\left(\frac{|x|}{2\alpha}\right) \right\}, \end{aligned} \quad (\text{A8})$$

where the expression contains the complementary error function  $\operatorname{erfc}(z) = 1 - \operatorname{erf}(z) = (2/\sqrt{\pi}) \int_0^z e^{-t^2} dt$ , we ob-



tain the final form of  $\psi_0(r, q)$

$$\begin{aligned} \psi_0(\mathbf{r}, \mathbf{q}) = & \frac{\pi}{L^2} \sum_j e^{i(\mathbf{q}+\mathbf{G}_j)\cdot\mathbf{r}} \left\{ \frac{4\alpha}{\sqrt{\pi}} \exp\left(-\frac{|\mathbf{G}_j+\mathbf{q}|}{4\alpha^2}\right) \right. \\ & \left. - 2|\mathbf{G}_j+\mathbf{q}| \operatorname{erfc}\left(\frac{|\mathbf{G}_j+\mathbf{q}|}{2\alpha}\right) \right\} \\ & + \left[ \frac{2\alpha e^{-\alpha^2|\mathbf{r}|^2}}{\sqrt{\pi}|\mathbf{r}|^2} - \frac{\operatorname{erf}(\alpha|\mathbf{r}|)}{|\mathbf{r}|^3} \right] \\ & + \sum_{j \neq 0} e^{-i\mathbf{q}\cdot\mathbf{R}_j} \left\{ \frac{\operatorname{erfc}(\alpha|\mathbf{R}_j+\mathbf{r}|)}{|\mathbf{R}_j+\mathbf{r}|^3} \right. \\ & \left. + \left( \frac{2\alpha}{\sqrt{\pi}} \right) \frac{e^{-\alpha^2|\mathbf{R}_j+\mathbf{r}|^2}}{|\mathbf{R}_j+\mathbf{r}|^2} \right\}. \end{aligned} \quad (\text{A9})$$

Similarly,

$$\begin{aligned} \psi_{I1} = & \frac{\pi}{L^2} \sum_j e^{i(\mathbf{q}+\mathbf{G}_j)\cdot\mathbf{r}} e^{\mathbf{G}_j\cdot\mathbf{c}} \frac{2}{\sqrt{\pi}} \int_0^{\alpha^2} t^{-1/2} \\ & \times \exp\left(\frac{|\mathbf{G}_j+\mathbf{q}|^2}{4t} - l^2 t\right) dt + \frac{2}{\sqrt{\pi}} \sum_j e^{-i\mathbf{q}\cdot(\mathbf{R}_j+\mathbf{c})} \\ & \times \int_{\alpha^2}^{\infty} t^{1/2} \exp\left(-|\tilde{\mathbf{R}}_j+\mathbf{r}|^2 t\right) dt, \end{aligned} \quad (\text{A10})$$

by replacing  $t$  by  $w^{-2}$ , the first integration of above equation can be rewritten as

$$\int_{1/\alpha}^{\infty} 2w^{-2} \exp\left(-\frac{|\mathbf{G}_j+\mathbf{q}|^2}{4} w^2 - \frac{l^2}{w^2}\right) dw. \quad (\text{A11})$$

Using the integration

$$\begin{aligned} & \int_{1/\alpha}^{\infty} w^{-2} \exp\left(-\frac{|x|^2 w^2}{4} - \frac{y^2}{w^2}\right) dw \\ & = \frac{\pi}{4y} \left[ e^{-|x|y} \operatorname{erfc}\left(\frac{|x|}{2\alpha} - \alpha y\right) \right. \\ & \quad \left. - e^{|x|y} \operatorname{erfc}\left(\frac{|x|}{2\alpha} + \alpha y\right) \right], \end{aligned} \quad (\text{A12})$$

and Eq. (A7) we have the form of  $\psi_{I1}$

$$\begin{aligned} \psi_{I1} = & \frac{\pi}{L^2 l} \sum_j e^{i(\mathbf{q}+\mathbf{G}_j)\cdot\mathbf{r}} e^{i\mathbf{G}_j\cdot\mathbf{c}} \left[ e^{-|\mathbf{G}_j+\mathbf{q}|l} \operatorname{erfc}\left(\frac{|\mathbf{G}_j+\mathbf{q}|}{2\alpha}\right) \right. \\ & \left. - \alpha l \right] - e^{|\mathbf{G}_j+\mathbf{q}|l} \operatorname{erfc}\left(\frac{|\mathbf{G}_j+\mathbf{q}|}{2\alpha} + \alpha l\right) \\ & + \sum_j e^{-i\mathbf{q}\cdot(\mathbf{R}_j+\mathbf{c})} \left[ \frac{\operatorname{erfc}(\alpha|\tilde{\mathbf{R}}_j+\mathbf{r}|)}{|\tilde{\mathbf{R}}_j+\mathbf{r}|^3} \right. \\ & \left. + \left( \frac{2\alpha}{\sqrt{\pi}} \right) \frac{\exp\left(-\alpha^2|\tilde{\mathbf{R}}_j+\mathbf{r}|^2\right)}{|\tilde{\mathbf{R}}_j+\mathbf{r}|^2} \right]. \end{aligned} \quad (\text{A13})$$

In the same way, we transform  $\psi_{I2}$  as

$$\begin{aligned} \psi_{I2} = & \frac{\pi}{3L^2 l^3} \sum_j e^{i(\mathbf{q}+\mathbf{G}_j)\cdot\mathbf{r}} e^{i\mathbf{G}_j\cdot\mathbf{c}} \left\{ -\frac{4\alpha l}{\sqrt{\pi}} \right. \\ & \times \exp\left(-\frac{|\mathbf{G}_j+\mathbf{q}|^2}{4\alpha^2} - \alpha^2 l^2\right) + \left[ e^{-|\mathbf{G}_j+\mathbf{q}|l} \right. \\ & \times (|\mathbf{G}_j+\mathbf{q}|l+1) \operatorname{erfc}\left(\frac{|\mathbf{G}_j+\mathbf{q}|}{2\alpha}\right) \\ & \left. + e^{|\mathbf{G}_j+\mathbf{q}|l} (|\mathbf{G}_j+\mathbf{q}|l-1) \operatorname{erfc}\left(\frac{|\mathbf{G}_j+\mathbf{q}|}{2\alpha} + \alpha l\right) \right] \Big\} \\ & + \sum_j e^{-i\mathbf{q}\cdot(\mathbf{R}_j+\mathbf{c})} \left\{ \frac{\operatorname{erfc}(\alpha|\tilde{\mathbf{R}}_j+\mathbf{r}|)}{|\tilde{\mathbf{R}}_j+\mathbf{r}|^5} \right. \\ & \left. + \left( \frac{2\alpha}{3\sqrt{\pi}} \right) \frac{3+2\alpha^2|\tilde{\mathbf{R}}_j+\mathbf{r}|^2}{|\tilde{\mathbf{R}}_j+\mathbf{r}|^4} e^{-\alpha^2|\tilde{\mathbf{R}}_j+\mathbf{r}|^2} \right\}, \end{aligned} \quad (\text{A14})$$

where the integrations

$$\begin{aligned} & \int_{1/\alpha}^{\infty} w^{-4} \exp\left(-\frac{|x|^2 w^2}{4} - \frac{y^2}{w^2}\right) dw \\ & = \frac{1}{8y^3} \left\{ -4\alpha y \exp\left(-\frac{|x|^2}{4\alpha^2} - \alpha^2 y^2\right) \right. \\ & \quad + \sqrt{\pi} \left[ e^{-|x|y} (|x|y+1) \operatorname{erfc}\left(\frac{|x|}{2y} - \alpha y\right) \right. \\ & \quad \left. \left. + e^{|x|y} (|x|y-1) \operatorname{erfc}\left(\frac{|x|}{2y} + \alpha y\right) \right] \right\}, \end{aligned} \quad (\text{A15})$$

and

$$\begin{aligned} & \int_{\alpha^2}^{\infty} t^{3/2} \exp(|x|^2 t) dt \\ & = \frac{3\sqrt{\pi}}{4|x|^5} \operatorname{erfc}(\alpha|x|) + \frac{\alpha(3+2\alpha^2|x|^2)}{2|x|^4} \\ & \quad \times \exp(-\alpha^2|x|^2), \end{aligned} \quad (\text{A16})$$

are used. After simplifying, we obtain the rapid convergent form of  $\psi_I(\mathbf{r}, \mathbf{q})$  as

$$\begin{aligned} \psi_I(\mathbf{r}, \mathbf{q}) = & \frac{\pi}{L^2} \sum_j e^{i(\mathbf{q}+\mathbf{G}_j)\cdot\mathbf{r}} e^{i\mathbf{G}_j\cdot\mathbf{c}} \left\{ \frac{4\alpha}{\sqrt{\pi}} \exp\left(-\frac{|\mathbf{G}_j+\mathbf{q}|^2}{4\alpha^2} \right. \right. \\ & \left. \left. - \alpha^2 l^2\right) - |\mathbf{G}_j+\mathbf{q}| \left[ e^{-|\mathbf{G}_j+\mathbf{q}|l} \operatorname{erfc}\left(\frac{|\mathbf{G}_j+\mathbf{q}|}{2\alpha}\right) \right. \right. \\ & \left. \left. - \alpha l \right] + e^{|\mathbf{G}_j+\mathbf{q}|l} \operatorname{erfc}\left(\frac{|\mathbf{G}_j+\mathbf{q}|}{2\alpha} + \alpha l\right) \right\} \\ & + \sum_j e^{-i\mathbf{q}\cdot(\mathbf{R}_j+\mathbf{c})} \left\{ \frac{\operatorname{erfc}(\alpha|\tilde{\mathbf{R}}_j+\mathbf{r}|)}{|\tilde{\mathbf{R}}_j+\mathbf{r}|^3} \right. \\ & \left. + \left( \frac{2\alpha}{\sqrt{\pi}} \right) \frac{\exp\left(-\alpha^2|\tilde{\mathbf{R}}_j+\mathbf{r}|^2\right)}{|\tilde{\mathbf{R}}_j+\mathbf{r}|^2} \right\} \end{aligned}$$

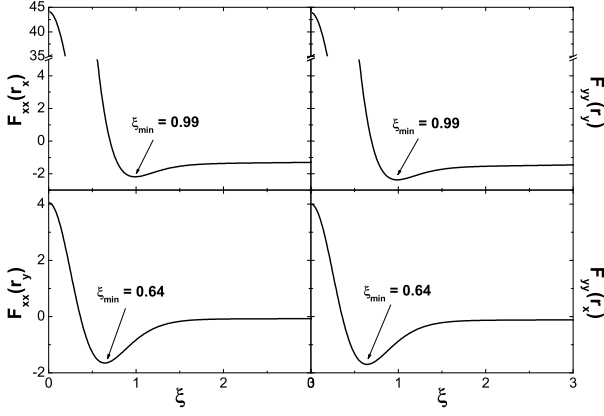


FIG. 13: (Color online) The quantities  $F_{xx}^r$ ,  $F_{yy}^r$ ,  $F_{xx}^r$  and  $F_{yy}^r$  as functions of  $\xi$ .

$$\begin{aligned}
 & -3l^2 \left[ \frac{\text{erfc}(\alpha|\tilde{\mathbf{R}}_j + \mathbf{r}|)}{|\tilde{\mathbf{R}}_j + \mathbf{r}|^5} \right. \\
 & + \left( \frac{2\alpha}{3\sqrt{\pi}} \right) \frac{3 + 2\alpha^2|\tilde{\mathbf{R}}_j + \mathbf{r}|^2}{|\tilde{\mathbf{R}}_j + \mathbf{r}|^4} \\
 & \left. \times \exp(-\alpha^2|\tilde{\mathbf{R}}_j + \mathbf{r}|^2) \right]. \quad (\text{A17})
 \end{aligned}$$

Therefore, the rapid convergent forms of  $E_0$  and  $E_I$  are expressed as Eqs. (4a) and (4b).

## APPENDIX B: INTERPRETATION OF THE MINIMA OF SOUND VELOCITIES FOR MH CONFIGURATION

For understanding the minimum of the LA and TA modes of the sound velocities of MH configuration, we define the following functions

$$\begin{aligned}
 F_{xx}^{r_x} &= \lim_{u_x \rightarrow 0} \frac{\partial^2 E_I}{\partial u_x^2} r_x^2, \\
 F_{xx}^{r_y} &= \lim_{u_x \rightarrow 0} \frac{\partial^2 E_I}{\partial u_x^2} r_y^2, \\
 F_{yy}^{r_x} &= \lim_{u_y \rightarrow 0} \frac{\partial^2 E_I}{\partial u_y^2} r_x^2, \\
 F_{yy}^{r_y} &= \lim_{u_y \rightarrow 0} \frac{\partial^2 E_I}{\partial u_y^2} r_y^2. \quad (\text{B1})
 \end{aligned}$$

Where  $E_I$  is the interaction potential between a dipole at origin and the dipoles in the opposite layer,  $u_{x(y)}$  is the  $x(y)$  component of the displacements of the origin dipole around its equilibrium position,  $r_{x(y)}$  is the  $x(y)$  component of the distance between the origin dipole and the dipoles in the opposite layer.

The first two plots in Fig. 13 describe  $F_{xx}^{r_x}$  and  $F_{yy}^{r_y}$ , as functions of  $\xi$ , which represent that the direction of vibration is along the direction of propagation. We find

that the minimum happens at the same value of  $\xi$  in the curves of  $F_{xx}^{r_x}$  and  $F_{yy}^{r_y}$  with in the plot of  $v_{\text{LA}}$  (see Fig. 5(a)), where  $\xi_{\text{min}} \approx 1$ . The rest two plots of Fig. 13 show  $F_{xx}^{r_y}$  and  $F_{yy}^{r_x}$  vs  $\xi$ , which express that the direction of vibration is perpendicular to the direction of propagation, the value of  $\xi$  the minimum arise at in this two curves is the same as in  $v_{\text{TA}}$  (see Fig. 5(b)), where  $\xi_{\text{min}} = 0.64$ . Due to the intrinsic property of interlayer dipole-dipole interaction, the four functions above have minima at  $\xi_{\text{min}} \approx 1$  and  $\xi_{\text{min}} = 0.64$  respectively.

## APPENDIX C: CORRELATION FUNCTIONS FOR BILAYER SYSTEM

From the Fourier transformation we know that the  $\gamma^{\text{th}}$  component of the displacement vectors of a dipole at the origin position in layer + and at the  $h^{\text{th}}$  nearest neighbor position in layer  $\sigma$  are

$$\begin{aligned}
 u_{\gamma}^{+}(0) &= \frac{1}{\sqrt{N}} \sum_{\mathbf{q}, j} c_{\gamma}^{+}(\mathbf{q}, j) \rho_{\gamma}^{+}(\mathbf{q}, j), \\
 u_{\gamma}^{\sigma}(h) &= \frac{1}{\sqrt{N}} \sum_{\mathbf{q}, j} c_{\gamma}^{\sigma}(\mathbf{q}, j) \rho_{\gamma}^{\sigma}(\mathbf{q}, j) \exp(i\mathbf{q} \cdot \mathbf{R}_h^{\sigma}), \quad (\text{C1})
 \end{aligned}$$

where  $\rho_{\gamma}^{\sigma}(\mathbf{q}, j)$  is the  $\gamma$  component of the eigenvector of  $j^{\text{th}}$  mode at  $\mathbf{q}$  point in the first Brillouin zone of the sublattice in layer  $\sigma = \pm$ .  $c_{\gamma}^{\sigma}(\mathbf{q}, j)$  is the probability parameter of  $\rho_{\gamma}^{\sigma}(\mathbf{q}, j)$ ,  $\mathbf{R}_h^{\sigma}$  is the relative position of the  $h^{\text{th}}$  nearest neighbor dipole in layer  $\sigma$ . Making use of the relation  $\langle c_{\gamma}^{\sigma}(\mathbf{q}, j) c_{\gamma'}^{\sigma'}(\mathbf{q}', j') \rangle = (k_B T / m \omega^2(\mathbf{q}, j)) \delta_{\mathbf{q}, \mathbf{q}'} \delta_{j, j'}$ , we can obtain the relative mean square displacements between the two considered nearest neighbors

$$\begin{aligned}
 & \langle |u_{\gamma}^{+}(0) - u_{\gamma}^{+}(h)|^2 \rangle \\
 &= \frac{2k_B T}{Nm} \sum_{\mathbf{q}, j} \frac{1}{\omega^2(\mathbf{q}, j)} \left\{ [\rho_{\gamma}^{+}(\mathbf{q}, j)]^2 (1 - \cos \mathbf{q} \cdot \mathbf{R}_h^{+}) \right\}, \quad (\text{C2a})
 \end{aligned}$$

$$\begin{aligned}
 & \langle |u_{\gamma}^{+}(0) - u_{\gamma}^{-}(h)|^2 \rangle \\
 &= \frac{k_B T}{Nm} \sum_{\mathbf{q}, j} \frac{1}{\omega^2(\mathbf{q}, j)} \left\{ [\rho_{\gamma}^{+}(\mathbf{q}, j)]^2 + [\rho_{\gamma}^{-}(\mathbf{q}, j)]^2 \right. \\
 & \quad \left. - 2 [\rho_{\gamma}^{+}(\mathbf{q}, j) \rho_{\gamma}^{-}(\mathbf{q}, j)] \cos(\mathbf{q} \cdot \mathbf{R}_h^{-}) \right\}, \quad (\text{C2b})
 \end{aligned}$$

where  $u_{\gamma}^{+}(0)$  and  $u_{\gamma}^{+(-)}(h)$  are the  $\gamma$  component of the original and the  $h^{\text{th}}$  nearest neighbor dipoles in the  $+$  ( $-$ ) layer,  $m$  is the mass of the dipoles,  $k_B$  is the Boltzmann constant,  $\omega(\mathbf{q}, j)$  is the phonon frequency of  $j^{\text{th}}$  mode at  $\mathbf{q}$  point in the first Brillouin zone. After the summation over the  $\gamma^{\text{th}}$  components and over the nearest neighbor sites, we can finally obtain the expressions Eqs. (13a) and (13b).

- 
- \* Electronic address: xglu@fudan.edu.cn
- <sup>1</sup> J. Stuhler, A. Griesmaier, T. Koch, M. Fattori, T. Pfau, S. Giovanazzi, P. Pedri, and L. Santos, Phys. Rev. Lett. **95**, 150406 (2005).
  - <sup>2</sup> T. Koch, T. Lahaye, J. Metz, B. Frhlich, A. Griesmaier, and T. Pfau, Nature Physics **4**, 218 (2008).
  - <sup>3</sup> D. Wang, J. Qi, M. F. Stone, O. Nikolayeva, H. Wang, B. Hattaway, S. D. Gensemer, P. L. Gould, E. E. Eyler, and W. C. Stwalley, Phys. Rev. Lett. **93**, 243005 (2004); J. M. Sage, S. Sainis, T. Bergeman, and D. DeMille, **94**, 203001 (2005); T. Rieger, T. Junglen, S. A. Rangwala, P. W. H. Pinkse, and G. Rempe, **95**, 173002 (2005); S. Hoekstra, J. J. Gilijamse, B. Sartakov, N. Vanhaecke, L. Scharfenberg, S. Y. T. van de Meerakker, and G. Meijer, **98**, 133001 (2007); W. C. Campbell, E. Tsikata, Hsin-I Lu, L. D. van Buuren, and J. M. Doyle, **98**, 213001 (2007); B. C. Sawyer, B. L. Lev, E. R. Hudson, B. K. Stuhl, M. Lara, J. L. Bohn, and J. Ye, **98**, 253002 (2007); S. Ospelkaus, A. Pe'er, K.-K. Ni, J. J. Zirbel, B. Neyenhuis, S. Kotochigova, P. S. Julienne, J. Ye, and D. S. Jin, arXiv:0802.1093; F. Lang, P. v. d. Straten, B. Brandstätter, G. Thalhammer, K. Winkler, P. S. Julienne, R. Grimm, and J. Hecker Denschlag, Nature Physics **4**, 223 (2008).
  - <sup>4</sup> See the upcoming book: *Cold molecules: Creation and applications*, edited by R. V. Krems, B. Friedrich and W. C. Stwalley, published by Taylor & Francis, London.
  - <sup>5</sup> B. Deb and L. You, Phys. Rev. A **64** (2001) 022717.
  - <sup>6</sup> A. V. Avdeenkov and J. L. Bohn, Phys. Rev. Lett. **90**, 043006 (2003).
  - <sup>7</sup> R. V. Krems, Phys. Rev. Lett. **96**, 123202 (2006).
  - <sup>8</sup> C. Ticknor and J. L. Bohn, Phys. Rev. A **72**, 032717 (2005).
  - <sup>9</sup> A. Derevianko, Phys. Rev. A **67** 033607 (2003); A. Derevianko, *Erratum*, Phys. Rev. A **72** 039901 (2005).
  - <sup>10</sup> S. Kotochigova and E. Tiesinga, Phys. Rev. A **73**, 041405(R) (2006).
  - <sup>11</sup> S. Kotochigova, Phys. Rev. Lett. **99**, 073003 (2007).
  - <sup>12</sup> A. Micheli, G. Pupillo, H. P. Büchler, and P. Zoller, Phys. Rev. A **76**, 043604 (2007).
  - <sup>13</sup> For studies in condensed matter setups see e.g.: D. Snoke, Science **298**, 1368 (2002); S. De Palo, F. Rapisarda, and G. Senatore, Phys. Rev. Lett. **88**, 206401 (2002); D. V. Kulakovskii, Yu. E. Lozovik, and A. V. Chaplik, JETP **99**, 850 (2004); G. J. Kalman, P. Hartmann, Z. Donko, and K. I. Golden, Phys. Rev. Lett. **98**, 236801 (2007), and references therein.
  - <sup>14</sup> D.-W. Wang, M. D. Lukin, and E. Demler, Phys. Rev. Lett. **97**, 180413 (2006).
  - <sup>15</sup> D.-W. Wang, Phys. Rev. Lett. **98**, 060403 (2007).
  - <sup>16</sup> L. Santos, G. V. Shlyapnikov, P. Zoller, and M. Lewenstein, Phys. Rev. Lett. **85**, 1791 (2000).
  - <sup>17</sup> D. S. Petrov, G. E. Astrakharchik, D. J. Papoular, C. Salomon, and G. V. Shlyapnikov, Phys. Rev. Lett. **99**, 130407 (2007).
  - <sup>18</sup> P. Pedri, S. De Palo, E. Orignac, R. Citro, and M. L. Chiofalo, Phys. Rev. A **77**, 015601 (2008).
  - <sup>19</sup> A. V. Gorshkov, P. Rabl, G. Pupillo, A. Micheli, P. Zoller, M. D. Lukin, and H. P. Büchler, arXiv:0805.0457
  - <sup>20</sup> D. H. J. O'Dell, S. Giovanazzi, and G. Kurizki, Phys. Rev. Lett. **90**, 110402 (2003).
  - <sup>21</sup> D.C.E. Bortolotti, S. Ronen, J.L. Bohn, and D. Blume, Phys. Rev. Lett. **97** (2006) 160402.
  - <sup>22</sup> H.P. Büchler, A. Micheli and P. Zoller, Nature Physics **3**, 726 (2007).
  - <sup>23</sup> M.A. Baranov, H. Fehrmann and M. Lewenstein, Phys. Rev. Lett. **100**, 200402 (2008).
  - <sup>24</sup> K. Góral, L. Santos, and M. Lewenstein, Phys. Rev. Lett. **88**, 170406 (2002).
  - <sup>25</sup> R. Barnett, D. Petrov, M. Lukin, and E. Demler, Phys. Rev. Lett. **96**, 190401 (2006).
  - <sup>26</sup> C. Menotti, C. Trefzger, and M. Lewenstein, Phys. Rev. Lett. **98**, 235301 (2007).
  - <sup>27</sup> C. Kollath, J. S. Meyer, and T. Giamarchi, Phys. Rev. Lett. **100**, 130403 (2008).
  - <sup>28</sup> E. G. Dalla Torre, E. Berg, and E. Altman, Phys. Rev. Lett. **97**, 260401 (2006).
  - <sup>29</sup> H. P. Büchler, E. Demler, M. D. Lukin, A. Micheli, N. V. Prokof'ev, G. Pupillo, and P. Zoller, Phys. Rev. Lett. **98**, 060404 (2007).
  - <sup>30</sup> G. E. Astrakharchik, J. Boronat, I. L. Kurbakov, and Yu. E. Lozovik, Phys. Rev. Lett. **98**, 060405 (2007).
  - <sup>31</sup> C. Mora, O. Parcollet, and X. Waintal, Phys. Rev. B **76**, 064511 (2007).
  - <sup>32</sup> A. S. Arkhipov, G. E. Astrakharchik, A. V. Belikov, Yu. E. Lozovik, JETP **82**, 41 (2005).
  - <sup>33</sup> C. Lee and E. A. Ostrovskaya, Phys. Rev. A **72**, 062321 (2005).
  - <sup>34</sup> R. Citro, E. Orignac, S. De Palo, and M. L. Chiofalo, Phys. Rev. A **75**, 051602(R) (2007)
  - <sup>35</sup> A. Micheli, G. K. Brennen, and P. Zoller, Nature Physics **2**, 341 (2006).
  - <sup>36</sup> G. K. Brennen, A. Micheli, and P. Zoller, New J. Phys. **9**, 138 (2007).
  - <sup>37</sup> G. Pupillo, A. Griessner, A. Micheli, M. Ortner, D.-W. Wang, and P. Zoller, Phys. Rev. Lett. **100**, 050402 (2008).
  - <sup>38</sup> S. F. Yelin, K. Kirby, and R. Côté, Phys. Rev. A **74**, 050301(R) (2006).
  - <sup>39</sup> E. Charron, P. Milman, A. Keller, and O. Atabek, Phys. Rev. A **75**, 033414 (2007).
  - <sup>40</sup> C. Lee and E. A. Ostrovskaya, Phys. Rev. A **72**, 062321 (2005).
  - <sup>41</sup> D. DeMille, Phys. Rev. Lett. **88**, 067901 (2002).
  - <sup>42</sup> P. Rabl, D. DeMille, J. M. Doyle, M.D. Lukin, R.J. Schoelkopf, and P. Zoller, Phys. Rev. Lett. **97**, 033003 (2006).
  - <sup>43</sup> P. Rabl and P. Zoller, Phys. Rev. A **76**, 042308 (2007).
  - <sup>44</sup> D.J. Wineland, C. Monroe, W.M. Itano, D. Leibfried, B.E. King, and D.M. Meekhof, J. Res. Natl. Inst. Stand. Tech. **103**, 259 (1998); E. Wigner, Phys. Rev. **46**, 1002 (1934).
  - <sup>45</sup> B. Groh and S. Dietrich, Phys. Rev. E **63**, 021203 (2001).
  - <sup>46</sup> G. Goldoni and F. M. Peeters, Phys. Rev. B **53**, 4591 (1996).
  - <sup>47</sup> A.A. Maradudin, E.W. Montroll, G.H. Weiss, and I.P. Ipatova, *Theory of lattice dynamics in the harmonic approximation* (Academic Press, New York, 1971), Suppl. 3.
  - <sup>48</sup> D. C. Wallace, *Thermodynamics of Crystals* (John Wiley & Sons, New York, 1972).
  - <sup>49</sup> V. M. Bedanov, G. V. Gadiyak, and Y. E. Lozovik, Phys. Lett. **109A**, 289 (1985).
  - <sup>50</sup> R. K. Kalia and P. Vashishta, J. Phys. C **14**, 643 (1981).
  - <sup>51</sup> D. S. Fisher, Phys. Rev. B **26**, 5009 (1982).